地球惑星観測・探査学／惑星探査学２
「惑星大気の電波観測」
Radio observations of planetary atmospheres

新領域創成科学研究科　複雑理工学専攻
今村　剛

Merit of radio observation

- Techniques of high-precision frequency measurements are available. This enables high-precision retrieval of atmospheric structures.
- Facilities for deep-space telecommunication can (sometimes) be used for the observations. This saves weight resources of spacecraft.

- Two types of observations are considered:
  - Radio occultation (active method)
  - Spectroscopy/radiometer (passive method)

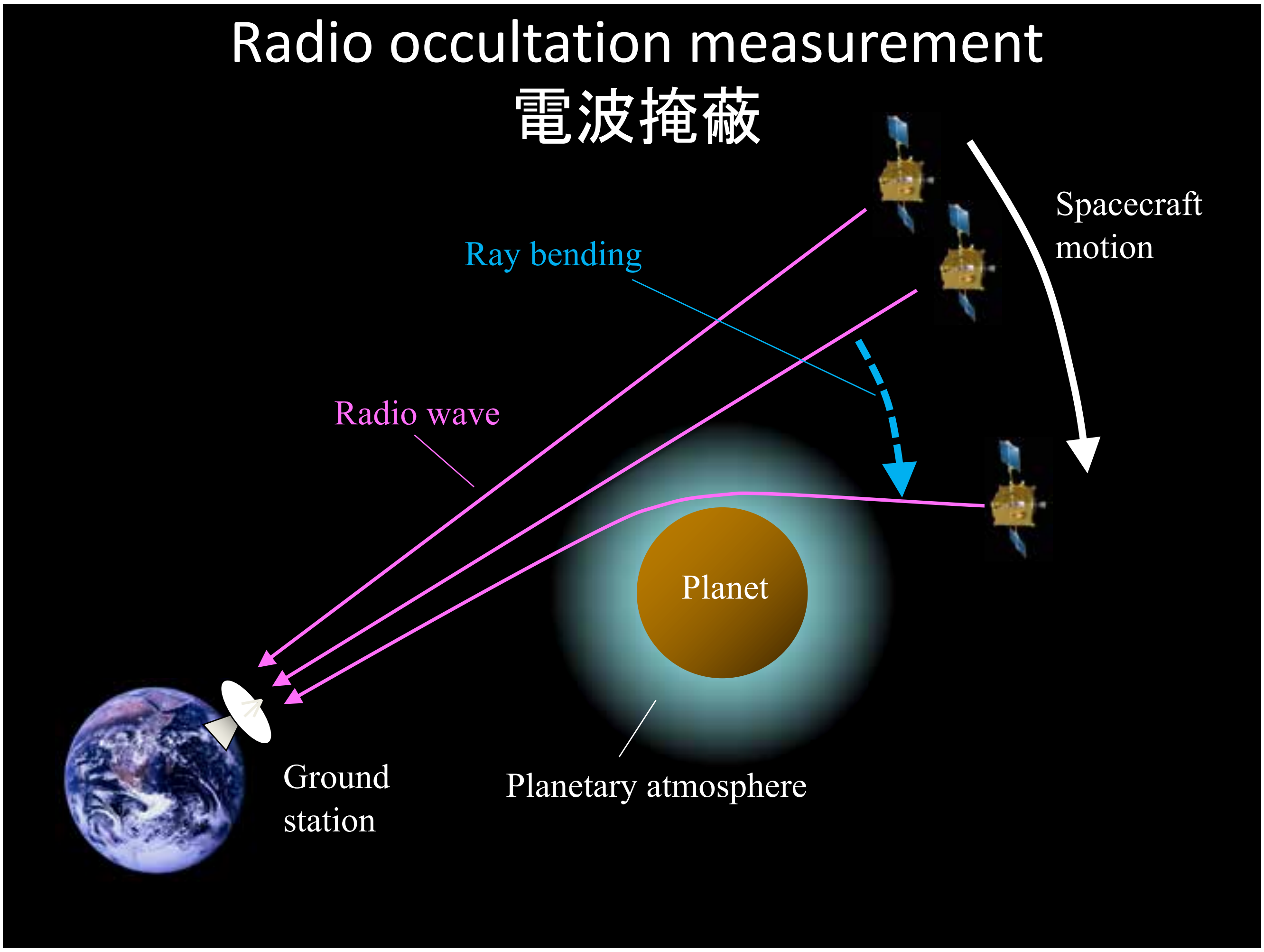

Ultra-Stable Oscillator (USO) on Akatsuki

Stability of USO after the launch

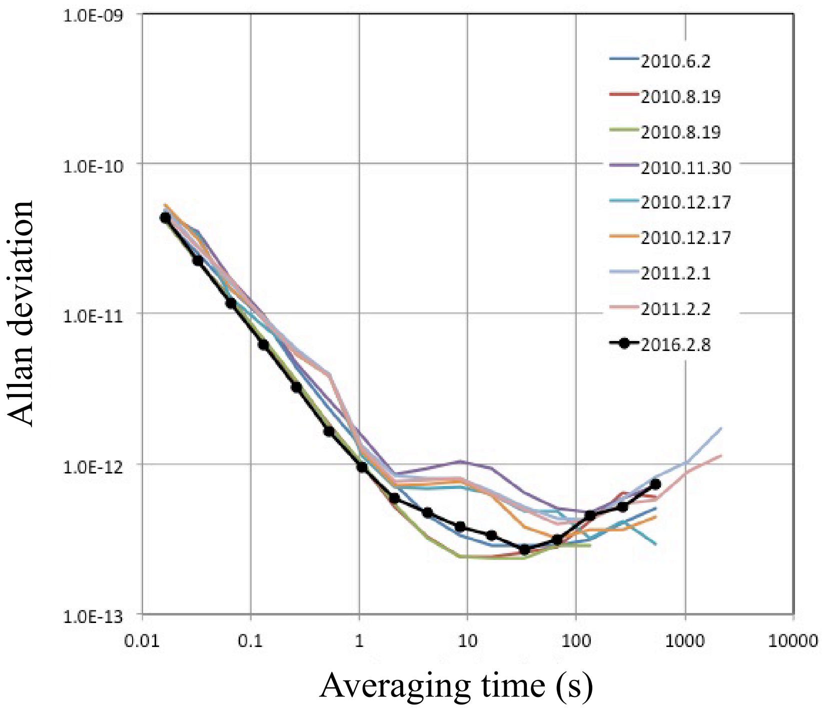


USO on Akatsuki

The requirement (Allan dev < 1×10^{-12} for τ = 1-1000 s) is satisfied.

Onboard telecommunication system

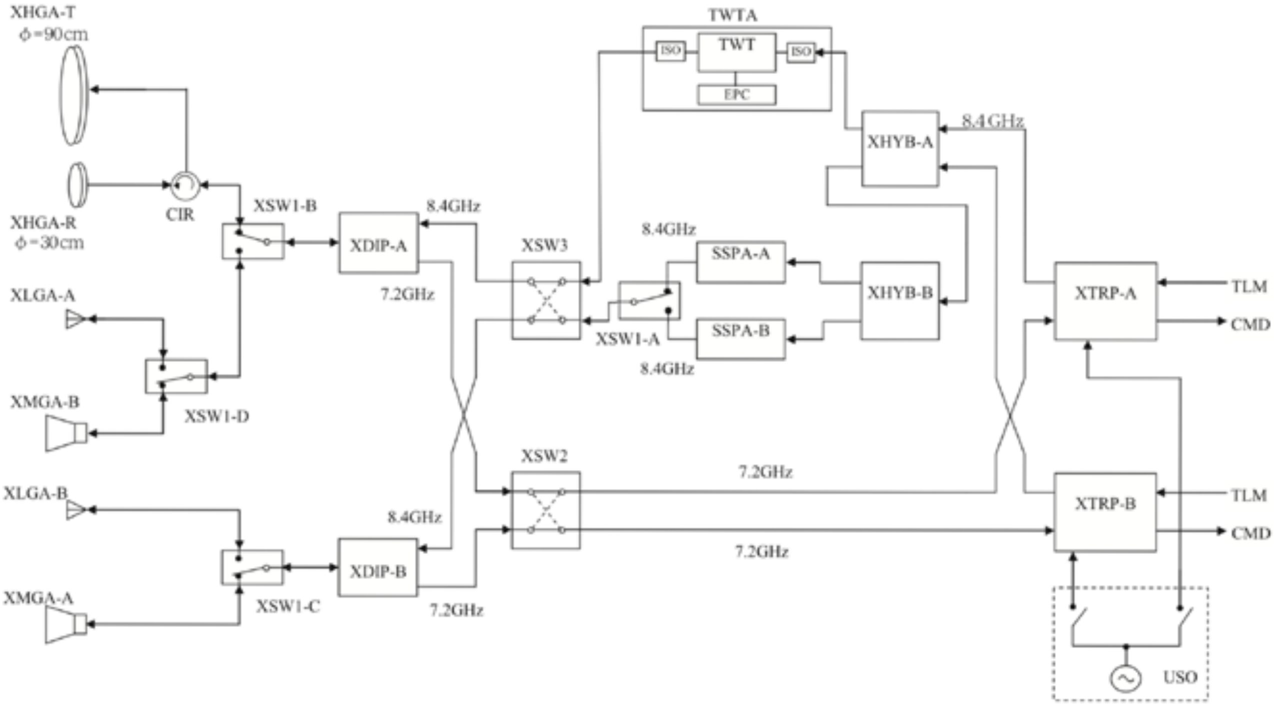

High-gain antenna

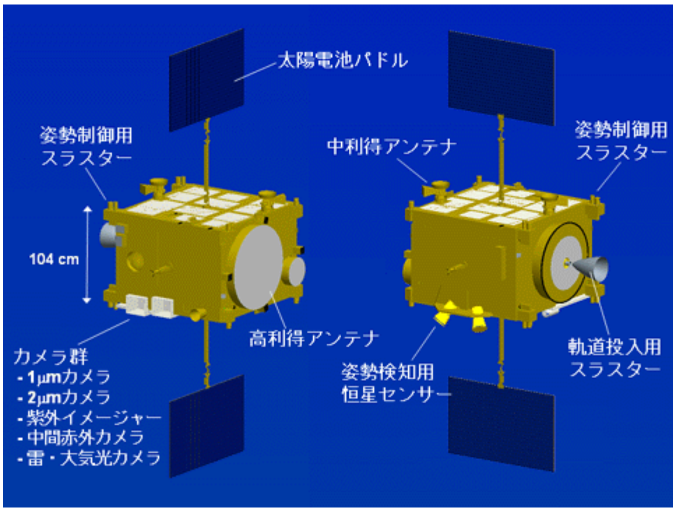

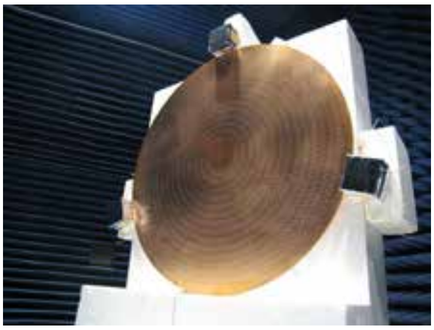

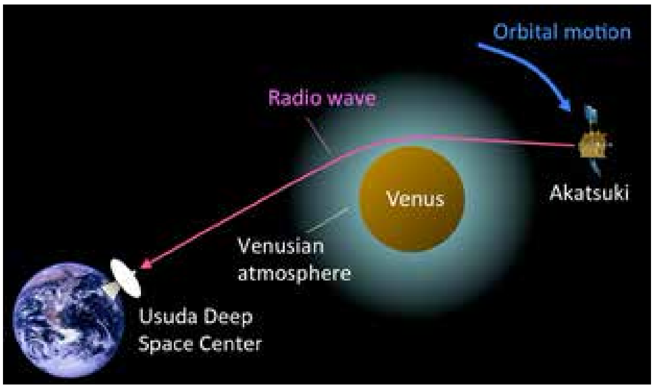

Attitude maneuver is needed during experiments due to ray bending

Data acquisition

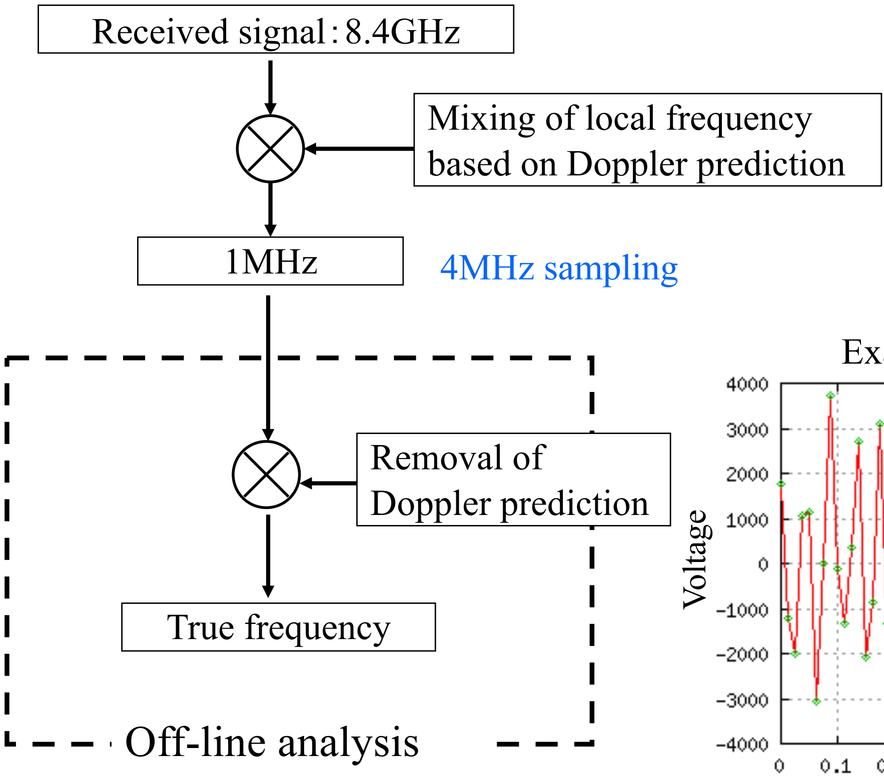

Usuda Deep Space Center (UDSC)

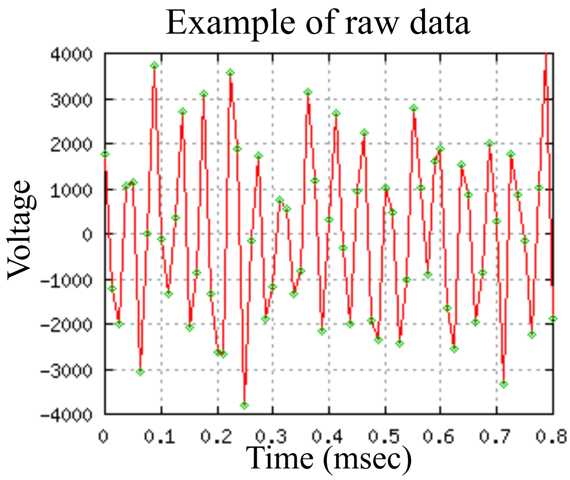

Spectrum of radio wave from Venus orbiter Akatsuki

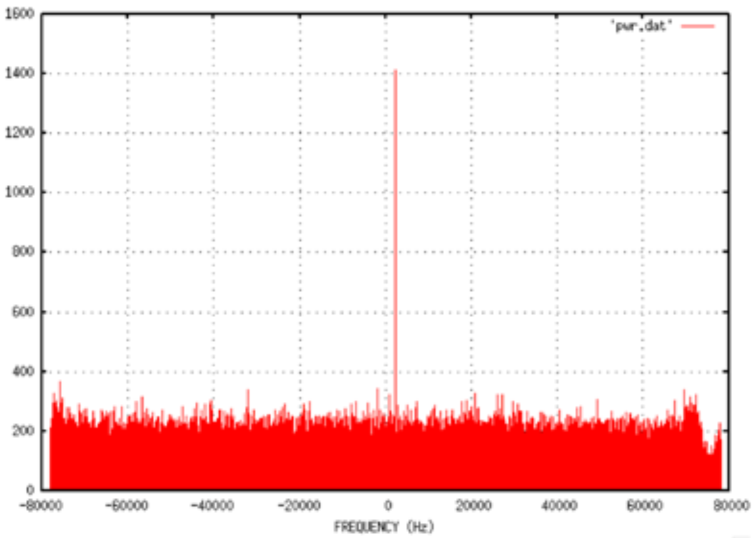

Signal spectrum with 1-sec integration reproduced from data in RDEF format at JAXA

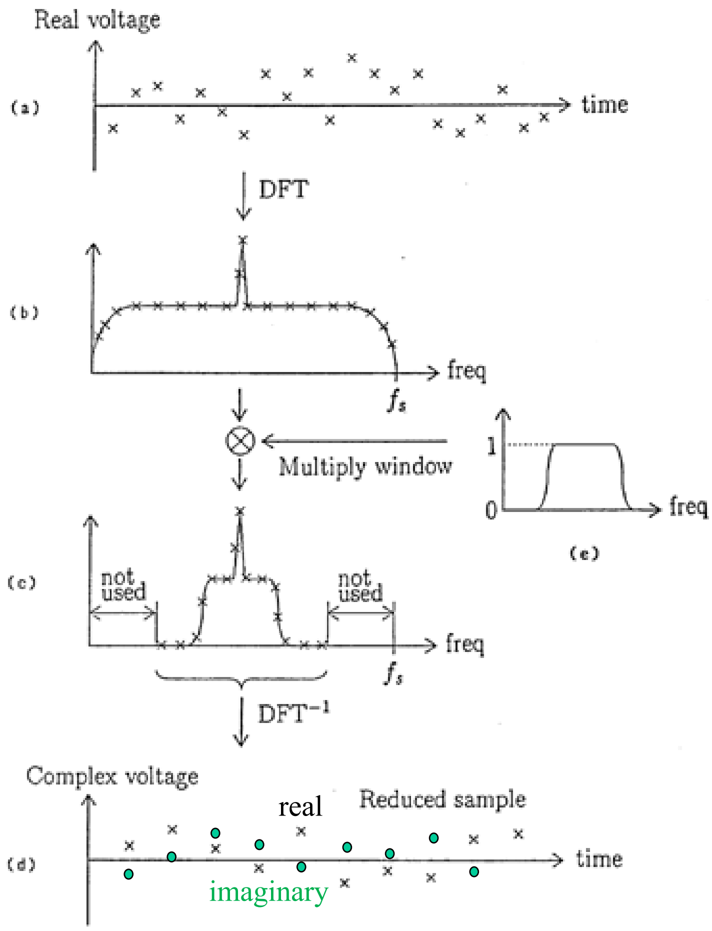

Filtering and decimation

Spectral fitting / Phase unwrapping

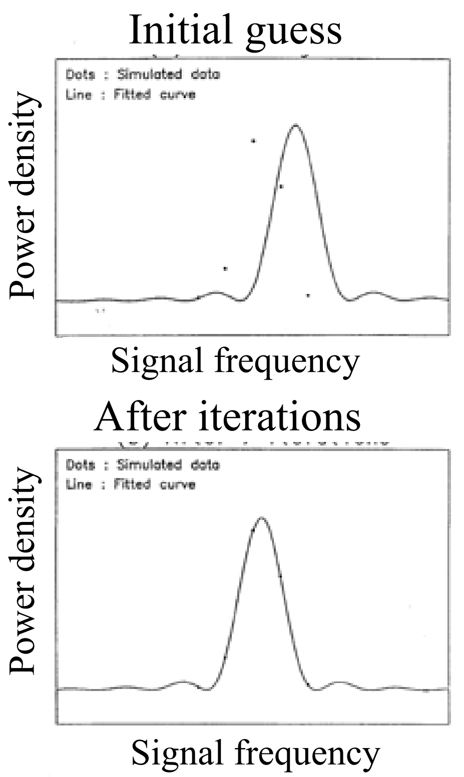

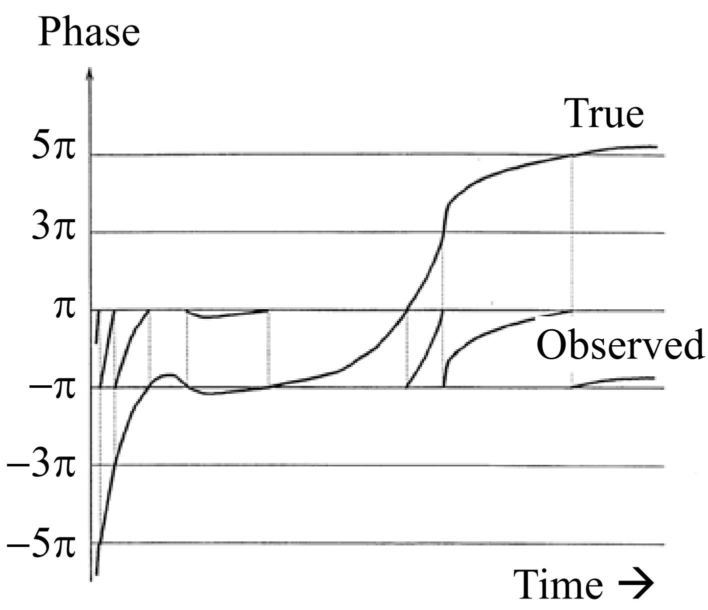

Radio occultation measurement

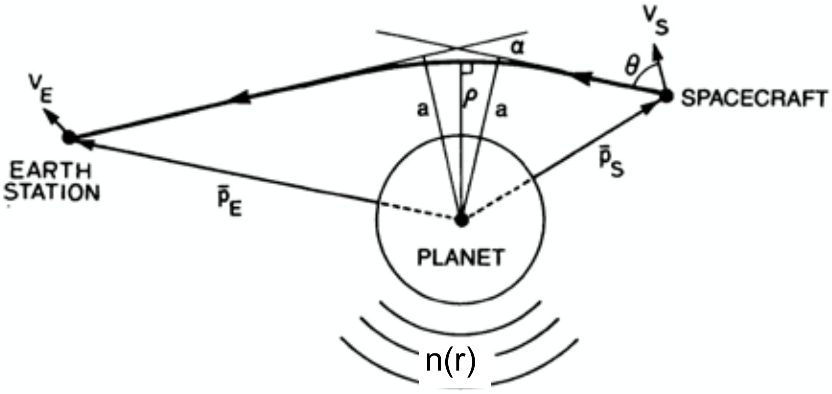

a : Impact parameter
α : Bending angle
n : Refractive index
r : Distance from planet center

Tyler (1987)

$$\alpha(a) = -2a \int_{r=r_0}^{r=\infty} \frac{1}{n}\frac{\partial n}{\partial r}\frac{dr}{\sqrt{(nr)^2 - a^2}}$$

Abel transformation:

$$\pi \ln n(r_{01}) = -\int_{a=a_1}^{a=\infty} \frac{\alpha(a)}{\sqrt{a^2 - a_1^{\,2}}}\,da$$

Refractive index n is related to atmospheric structure:

$$\mu(r) = (n(r)-1)\times 10^6$$: Refractivity

$$= \underbrace{\boxed{\kappa N_n(r)}}_{\text{neutral atmosphere}} - \underbrace{\boxed{40.3\frac{N_e(r)}{f_0^2}\times 10^6}}_{\text{plasma}}$$

Retrieval of the neutral atmosphere's temperature based on hydrostatic equilibrium:

$$T(r) = \frac{N_n(r_{top})}{N_n(r)}T(r_{top}) + \frac{\overline{m}}{kN_n(r)}\int_r^{r_{top}} N_n(r')g(r')dr$$

- Temperature at the upper boundary should be given from empirical models. The effect of the upper boundary almost disappears 1-2 scale heights below the boundary.

Retrieval procedure

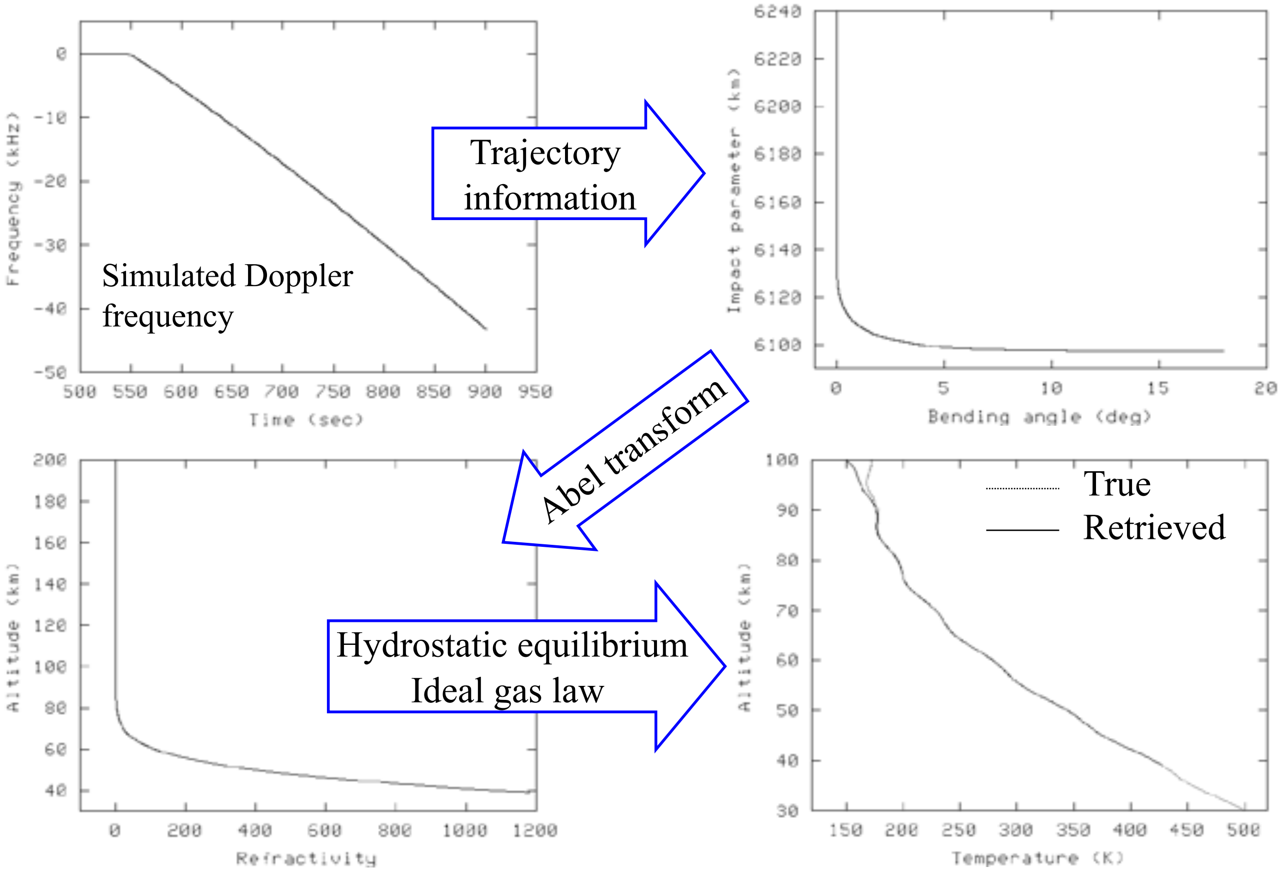

Temperature profiles of the Venus atmosphere obtained by Akatsuki radio occultation

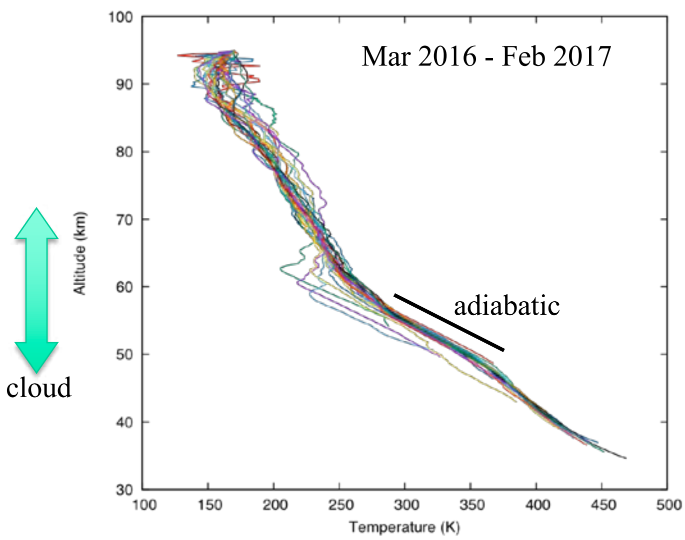

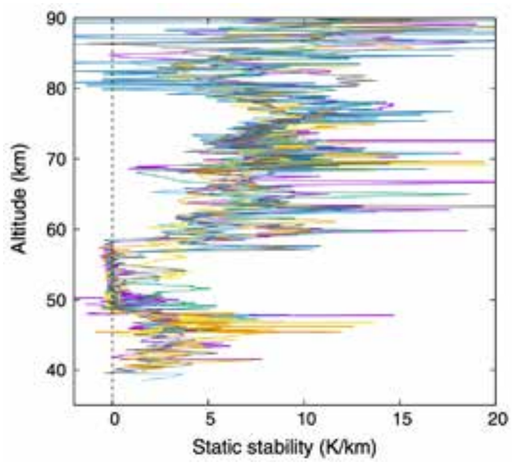

Imamura et al. 2017

static stability: $S = \dfrac{dT}{dz} - \dfrac{g}{c_p}$

T : temperature
z : altitude
g : gravitational acceleration
c_p : specific heat for constant pressure

Thermal structure below clouds revealed by Venus Express and Akatsuki radio occultation

static stability: $S = \dfrac{dT}{dz} - \dfrac{g}{c_p}$

T : temperature
z : altitude
g : gravitational acceleration
c_p : specific heat for constant pressure

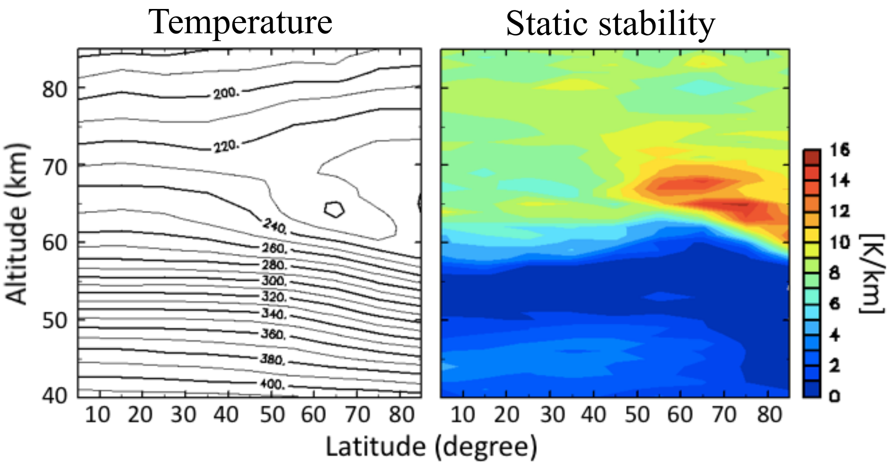

- Near-neutral layer extends to the sub-cloud region in the high latitude
- Unknow energy transport below clouds ?

Localtime dependence of static stability (< 40°)

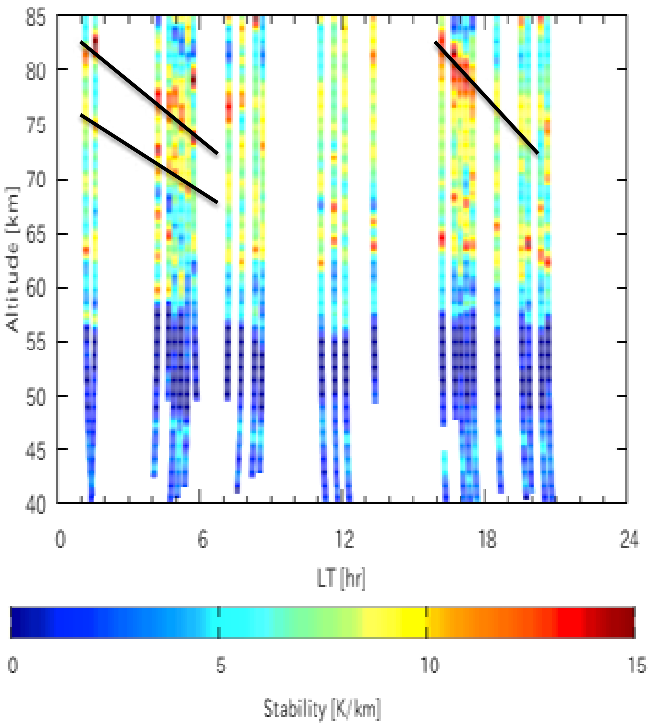

Static stability in Venus GCM

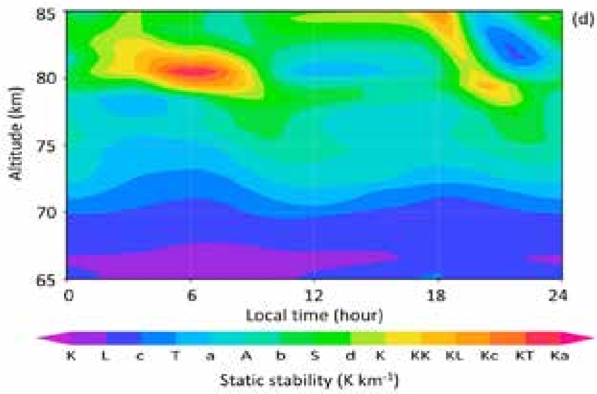

Ando, Takagi, et al. (2018)

Small-scale structures

Small-scale temperature fluctuations = Gravity waves ?
(Tellmann et al. 2012)

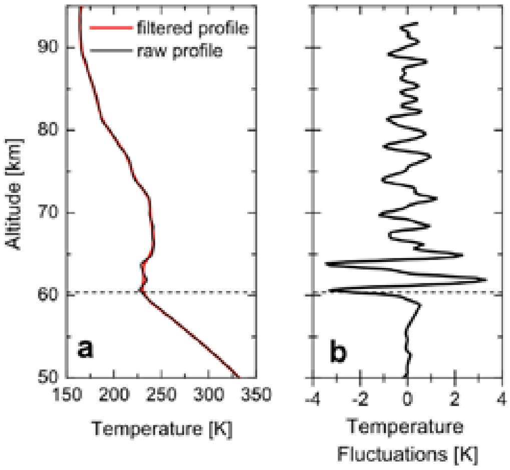

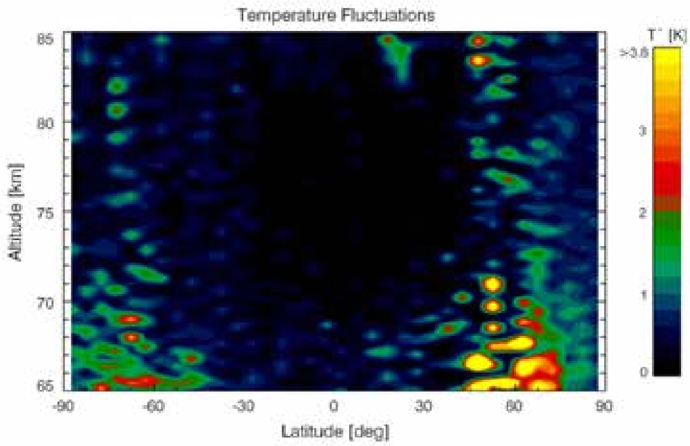

Radio occultation by Venus Express

Radio occultation of Martian atmosphere

Convective boundary layer on Mars (Hinson et al. 2008)

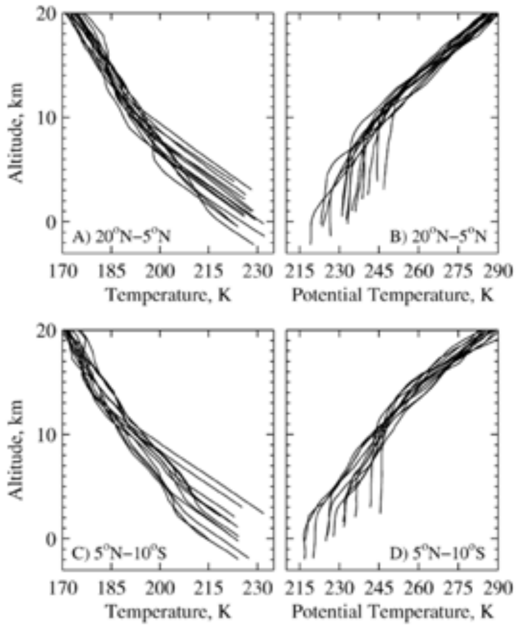

Fig. 2. Thermal structure of the tropical atmosphere as observed in MEX radio occultations. The top panels show profiles of (A) T and (B) θ from 14 experiments at latitudes of 20° N–5° N. The bottom panels show analogous profiles of (C) T and (D) θ from 12 experiments at latitudes of 5° N–10° S. Altitude is measured from the reference areoid used in defining surface elevation (e.g. Smith et al., 1999). The bottom of each profile is roughly 1 km above the local surface. These measurements are widely distributed in longitude, as shown in Fig. 1, but the local time remained essentially constant, about 17.1 h.

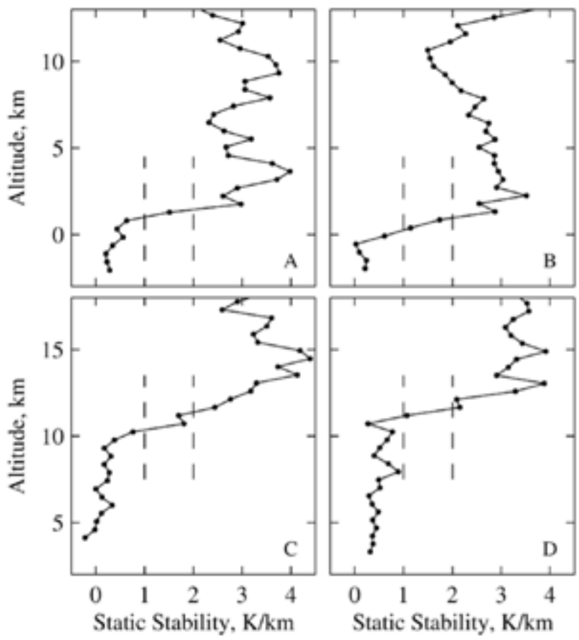

Fig. 3. Profiles of static stability S, as defined in Eq. (2), at four locations in the northern tropics: (A) 205° E, 22° N, (B) 205° E, 14° N, (C) 237° E, 12° N, and (D) 270° E, 8° N. The measurement locations are labeled a–d in Fig. 1. Samples of S were obtained at height intervals of about 500 m, as shown by the dots within each profile. Dashed vertical lines denote static stabilities of 1 and 2 K km^{-1}. Note that different vertical scales are used for the upper and lower pairs of profiles.

“Nocturnal mixed layer” on Mars

Hinson et al. (2014)

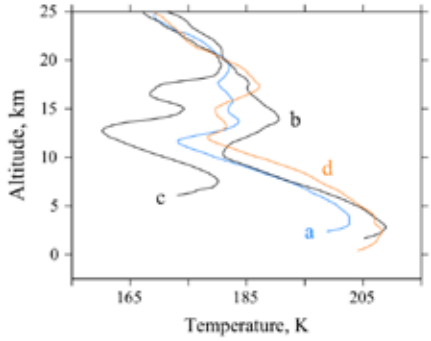

Fig. 5. Profiles of T for the same set of measurements as Fig. 4. The mixed layer in each profile resides between the mid-level and near-surface temperature inversions. The pressure at the top of the mixed layer is roughly 160 Pa.

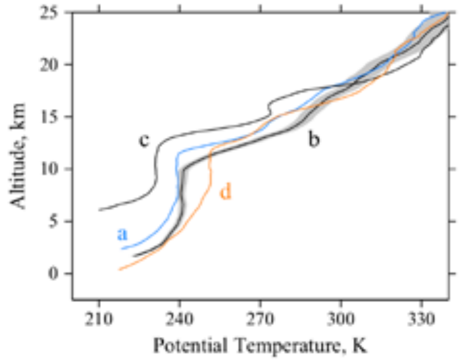

Fig. 4. MRO RO profiles of θ from four widely separated locations in the tropics: (a) 35°E, 4.7°S, (b) 125°E, 2.3°S, (c) 257°E, 2.2°S, and (d) 310°E, 4.9°N. The season is summer (L_s = 118–131°) and the local time is ~5 h. Each profile contains a detached mixed layer where θ is constant. The bottom of each profile is ~500 m above the surface. Altitude is measured from the reference areoid. The shaded region surrounding profile 'b' shows the typical 1-sigma uncertainty in θ for this set of observations.

High-altitude nighttime clouds and convection

Spiga et al. 2018

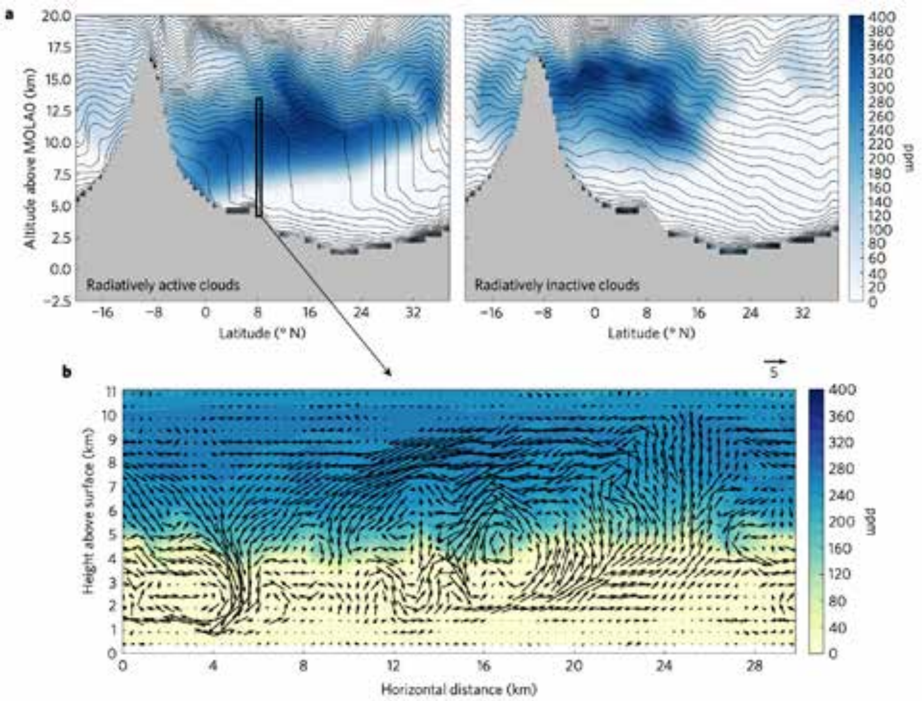

Figure 2 | The radiative effect of water-ice clouds at night triggers powerful convective plumes causing deep mixing layers and ice microbursts. **a**, Water-ice volumetric mixing ratio (shaded) and potential temperature (contours) simulated by mesoscale modelling with (top left) and without (top right) radiatively active water-ice clouds, at the longitude of Arsia Mons (−120° E), the season of the aphelion cloud belt (L_s = 120°), and the local time of radio-occultations (~3 AM). **b**, Typical water-ice volumetric mixing ratio (shaded) and convective winds (vectors, shown every two grid points) from LES with radiatively active water-ice clouds in environmental conditions corresponding to the region indicated in **a**.

limitation of vertical resolution

$$F_n = \sqrt{\frac{n\lambda d_1 d_2}{d_1 + d_2}}, \quad d_1, d_2 \gg n\lambda,^{[3]}$$

where

F_n is the nth Fresnel zone radius,
d_1 is the distance of P from one end,
d_2 is the distance of P from the other end,
λ is the wavelength of the transmitted signal.

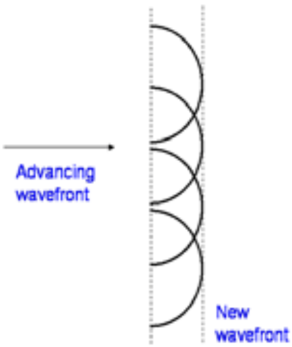

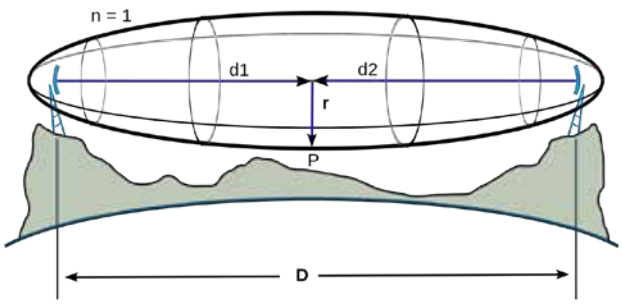

(Wikipedia)

n = 1 : First Fresnel zone. Outside this zone a destructive inference greatly reduces the contribution to the received signal.

F_1 is typically several hundred kilometers for interplanetary missions.

Multipath

An example of the signal spectrum time series

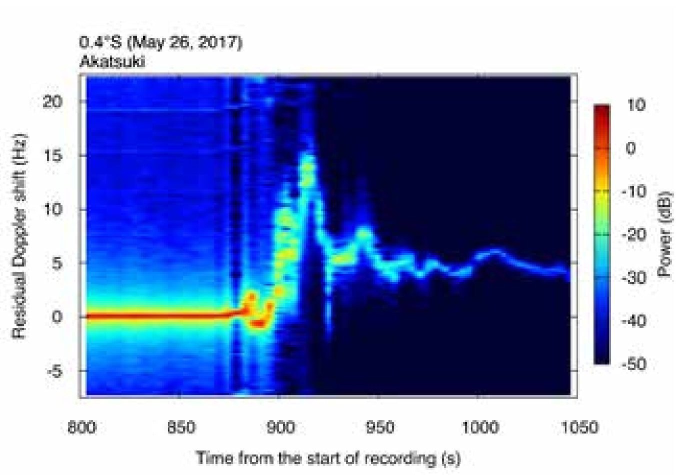

Schematic of multipath (Sokolovskiy, 2004)

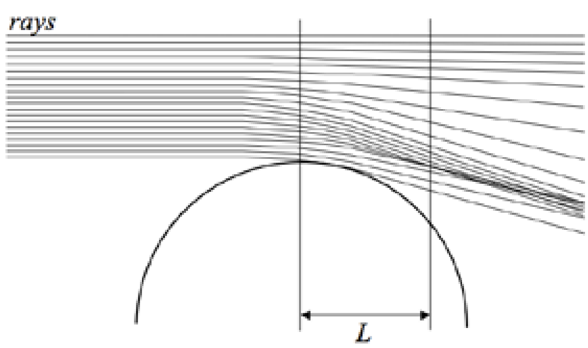

Radio holographic method can solve multipath problem (Imamura et al. 2018)

Radio holographic analysis

- One of the radio holographic methods, FSI ("Full Spectrum Inversion" Jensen et al. 2003) is applied to RS data.
- Spectral analysis is applied to the entire signal at once instead of applying it to successive short time blocks.
  →High vertical resolution + Disentanglement of multipath

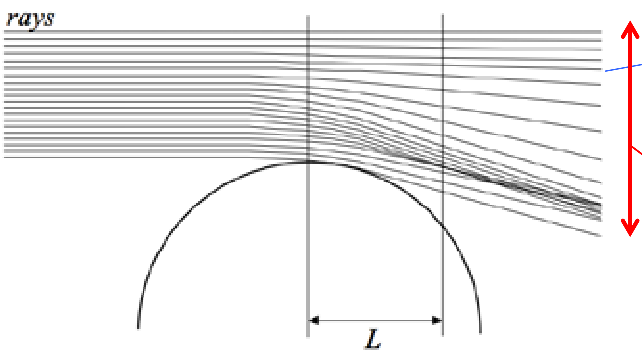

GO (geometrical optics) solves the instantaneous ray path at each time step

FSI solves the whole time series of the signal phase at once

Schematic of multipath (Sokolovskiy, 2004)

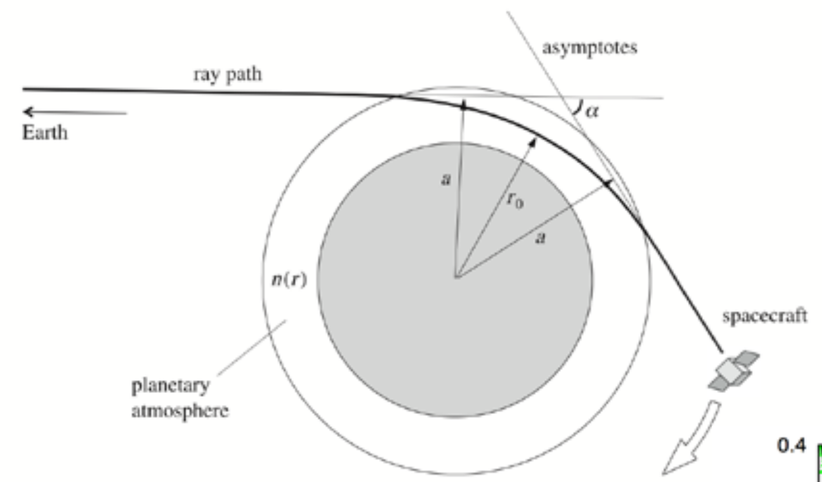

Abel transform to obtain the refractive index profile

$$\ln n(r) = -\frac{1}{\pi}\int_{a_1}^{\infty} \ln\left\{\frac{a}{a_1} + \left[\left(\frac{a}{a_1}\right)^2 - 1\right]^{\frac{1}{2}}\right\}\frac{d\alpha}{da}da$$

α needs to be a single-valued function of a.

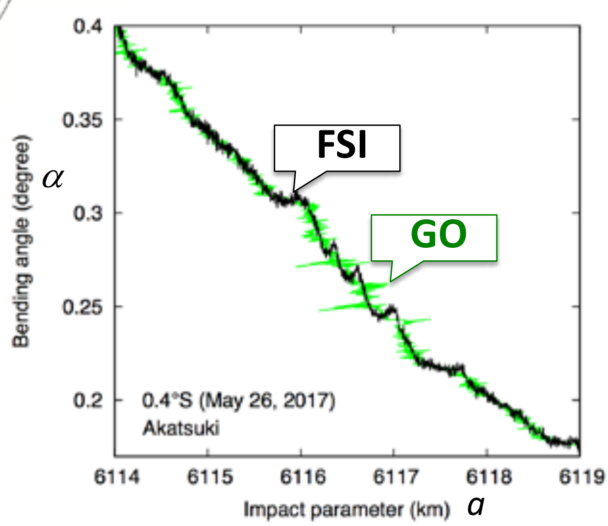

Examples

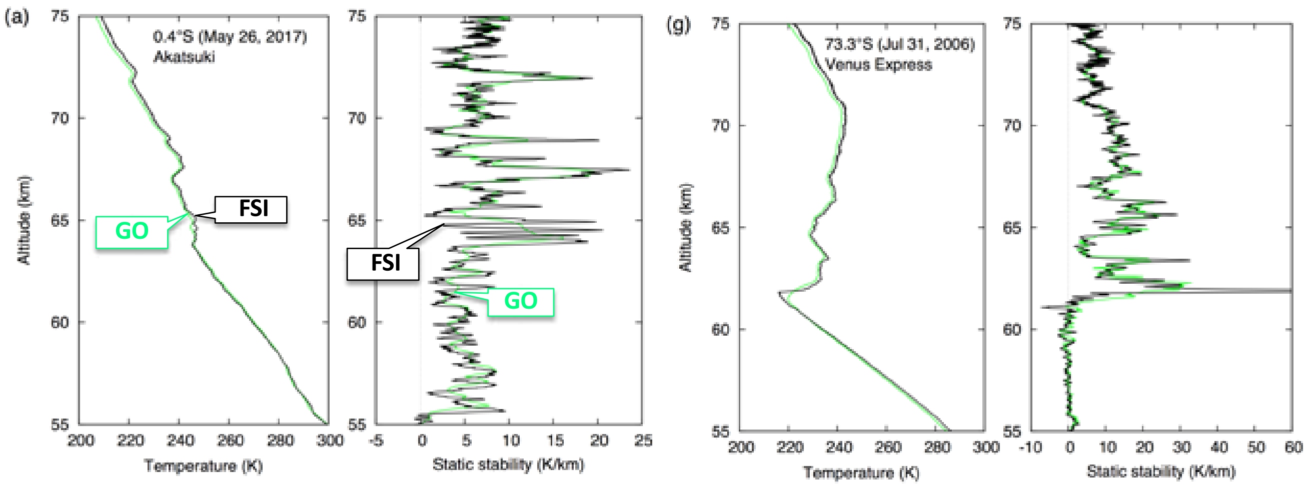

Imamura et al. (2018)

Radio occultation measurements of Pluto's neutral atmosphere with New Horizons

- Pluto has a tenuous atmosphere composed primarily of N_2.
- New Horizons spacecraft performed a radio occultation that sounded Pluto's atmosphere In 2015.
- Signals were transmitted by four antennas of the NASA Deep Space Network, and the spacecraft received the signals. The data streams were digitized, filtered, and stored on the spacecraft for later transmission to Earth.

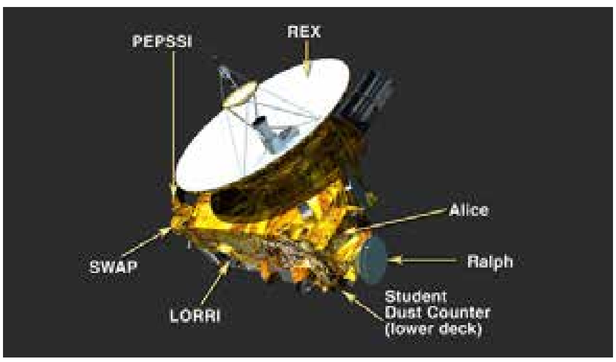

Hinson et al. (2017)

removal of diffraction effects caused by the surface of Pluto

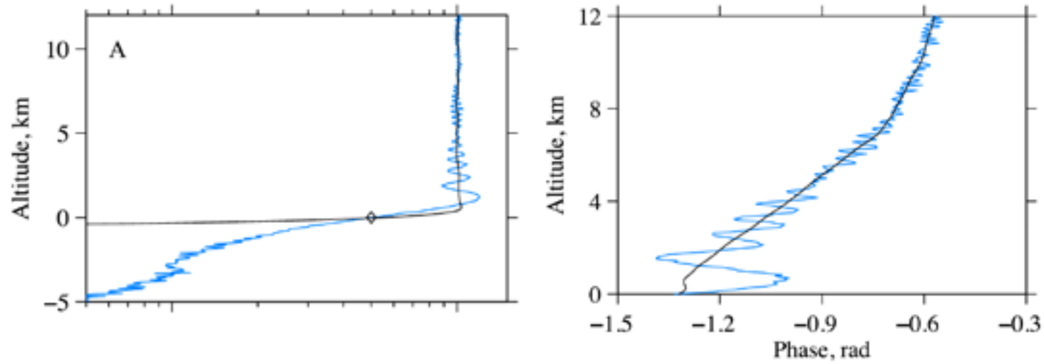

atmospheric profiles

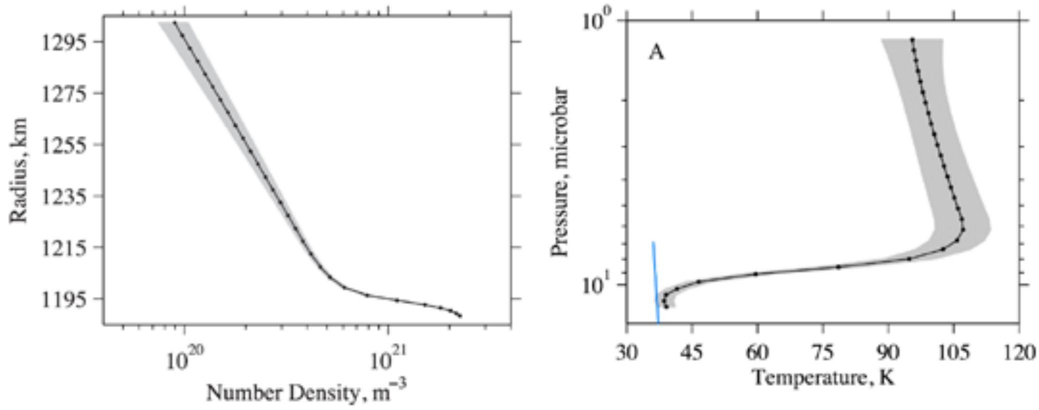

Radio occultation of lunar photoelectron layer with SELENE

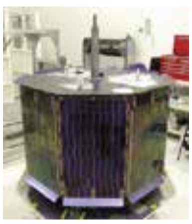

Vstar subsatellite

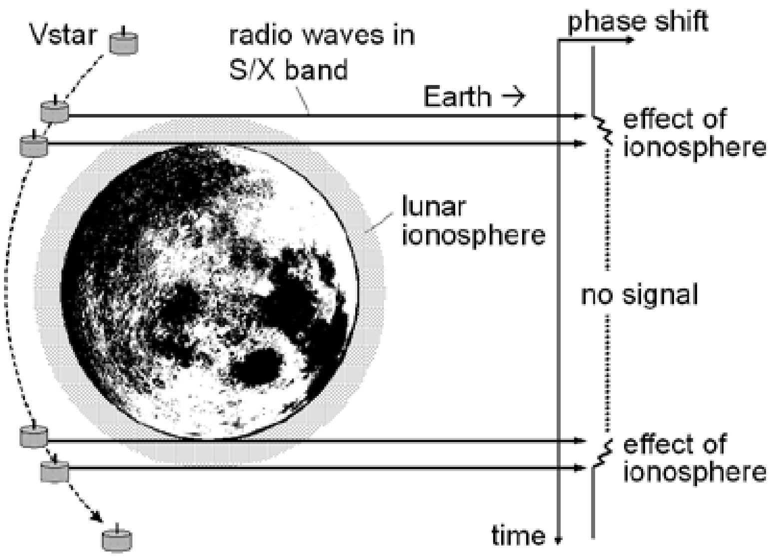

Usuda Deep Space Center, Japan

Dual-frequency method

To remove the effect of the fluctuation of the transmitted signal’s frequency and the neutral atmosphere’s contribution, two frequencies generated from the common onboard oscillator are used. A linear combination of these phases can extract the plasma contribution.

$$\Delta\phi_S = -\frac{40.3}{c\, f_S} N_e + \alpha\, f_S$$: Phase shift of S-band

$$\Delta\phi_X = -\frac{40.3}{c\, f_X} N_e + \alpha\, f_X$$: Phase shift of X-band

$$\delta\phi = \Delta\phi_S - \frac{f_S}{f_X}\Delta\phi_X = -\frac{40.3}{c} f_S \left(\frac{1}{f_S^2} - \frac{1}{f_X^2} \right) \cdot N_e$$: Differential phase

Analysis procedure

Phase deviation in S-band (ϕ_S) and X-band (ϕ_X)

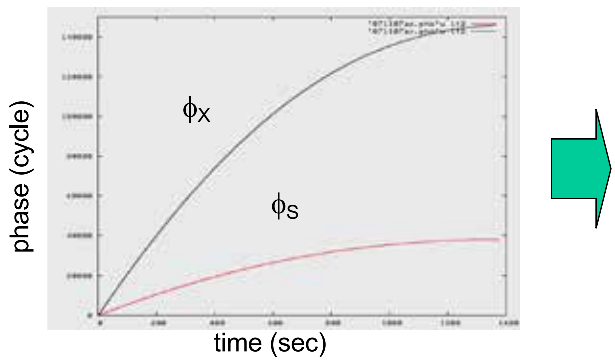

Differential phase $\phi_{diff} = \phi_S - f_s/f_x\, \phi_X$
(f_s, f_x : S/X-band nominal freq.)

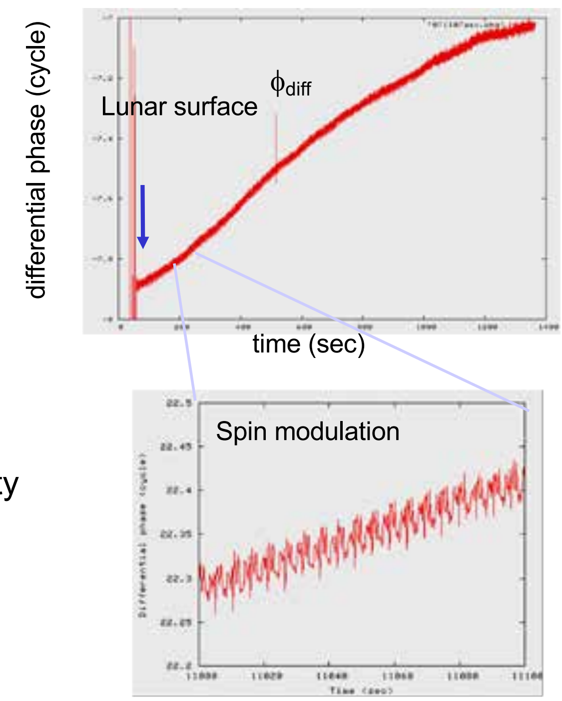

ϕ_{diff} is proportional to the electron density integrated along the ray path.

Mean density profile at SZA<60°

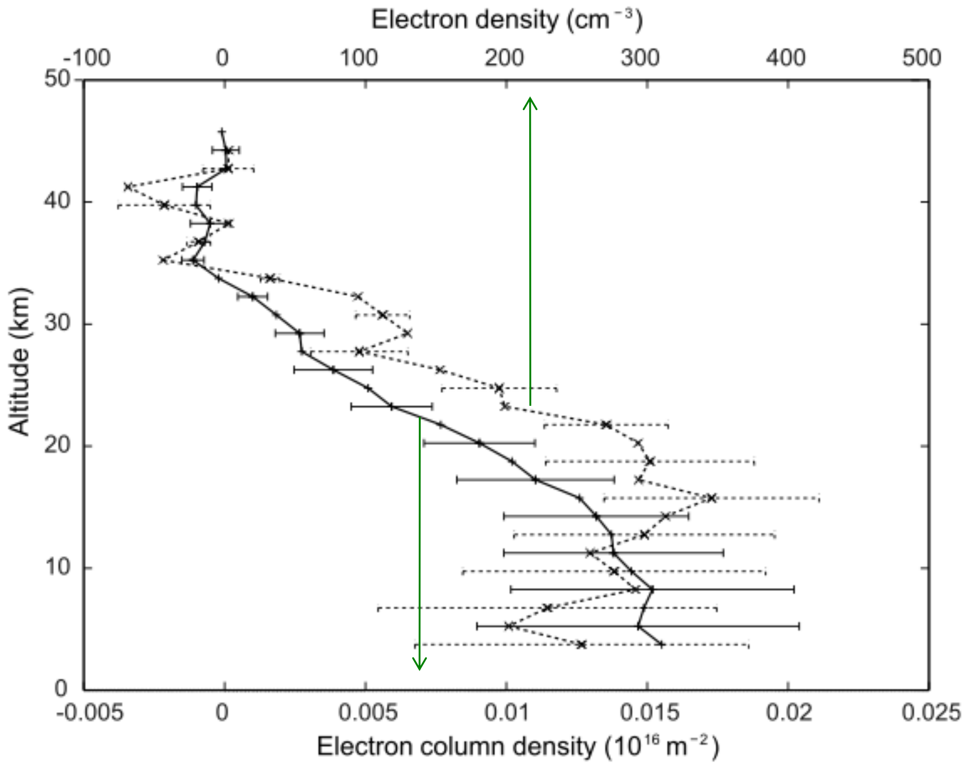

Imamura et al. (2012, JGR)

Examples of Venus' electron density profile from Akatsuki radio occultation

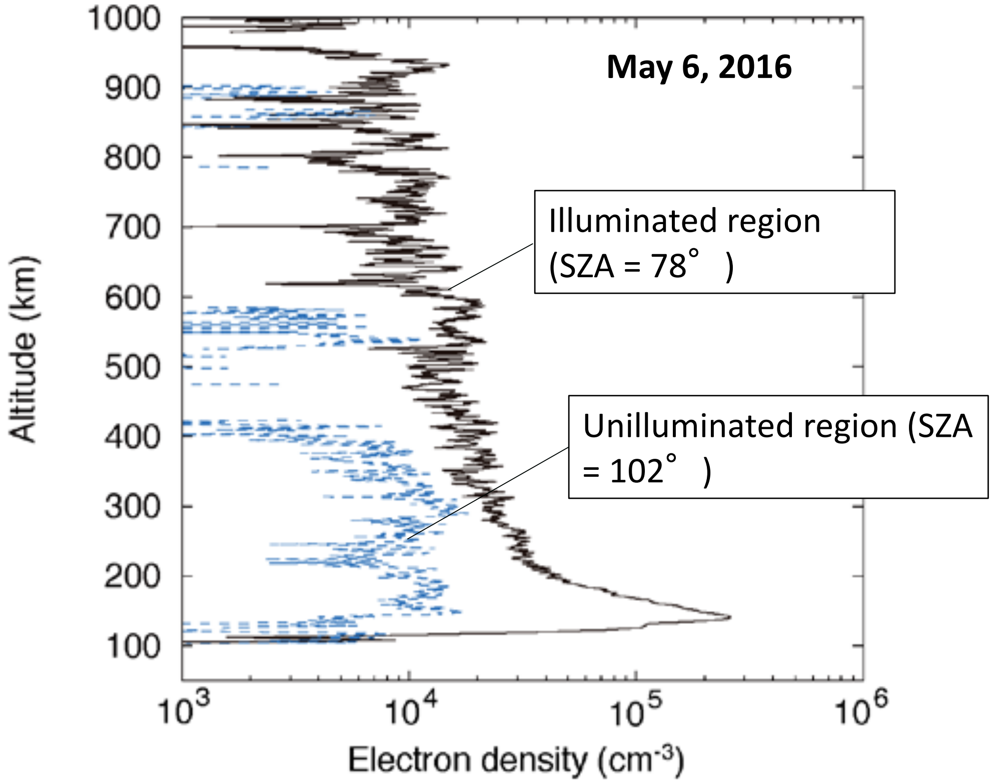

GPS meteorology for Earth

UCAR/COSMIC homepage

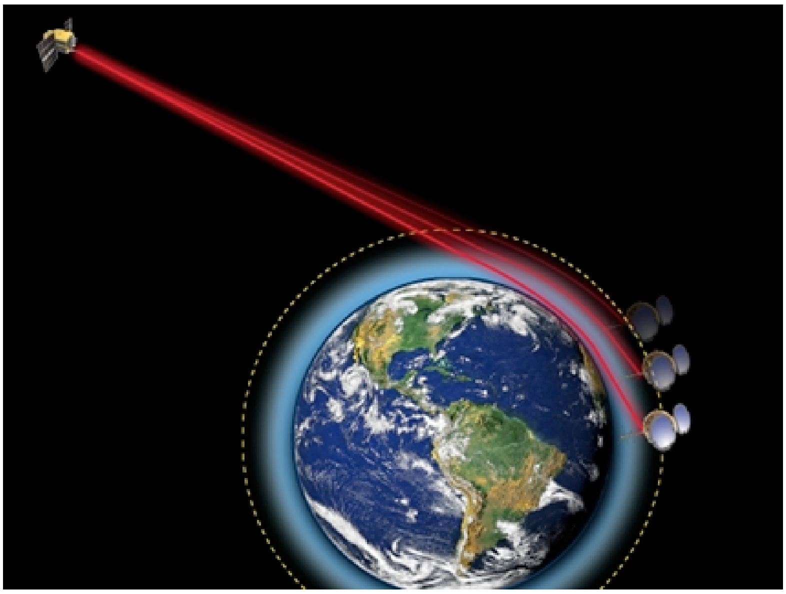

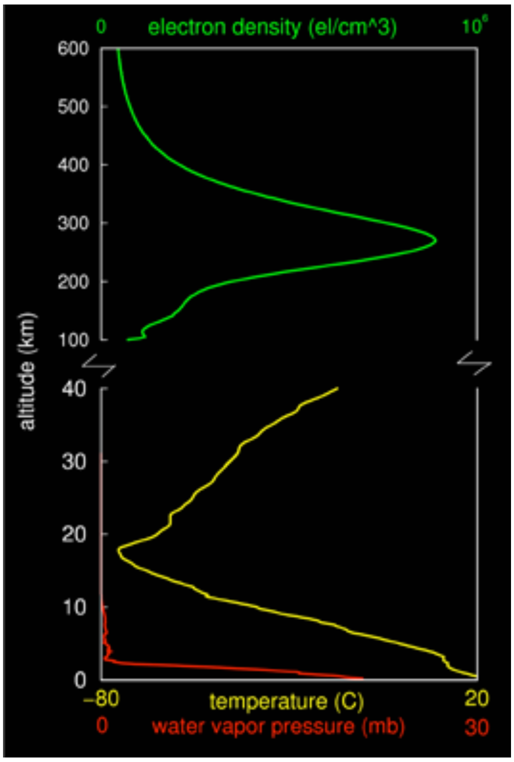

COSMIC : Constellation Observing System for Meteorology, Ionosphere, and Climate

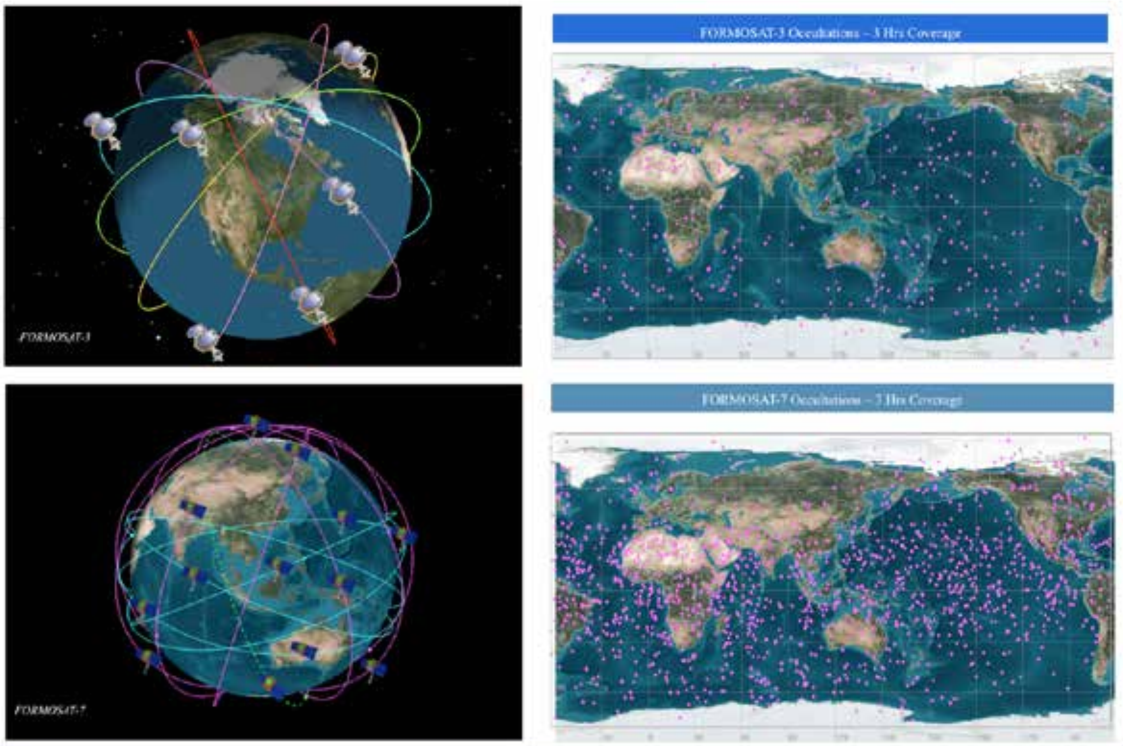

UCAR/COSMIC homepage

Fig. 1. Constellation design and estimated distribution of GPS RO soundings over a 3-h period from COSMIC/FORMOSAT-3 and COSMIC-2/FORMOSAT-7. The first tropical constellation of COSMIC-2 will be launched in 2016, and the second constellation will be launched in 2018. COSMIC-2 will provide an order of magnitude more GPS RO soundings over the tropics, which will have a significant impact on tropical cyclone prediction.

Dual-orbiter planetary mission

Satellite-to-satellite radio occultation and atmospheric spectroscopy for understanding vertical transport of water, dust and minor gases which controls climate evolution

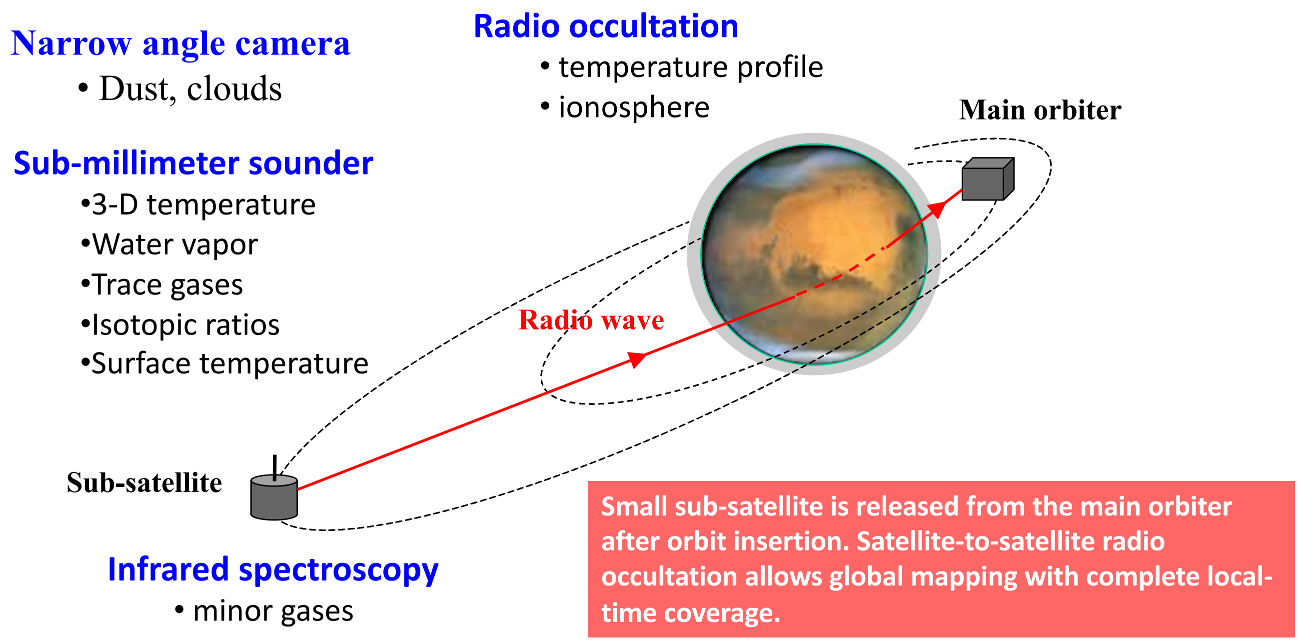

Signal intensity time series (Akatsuki)

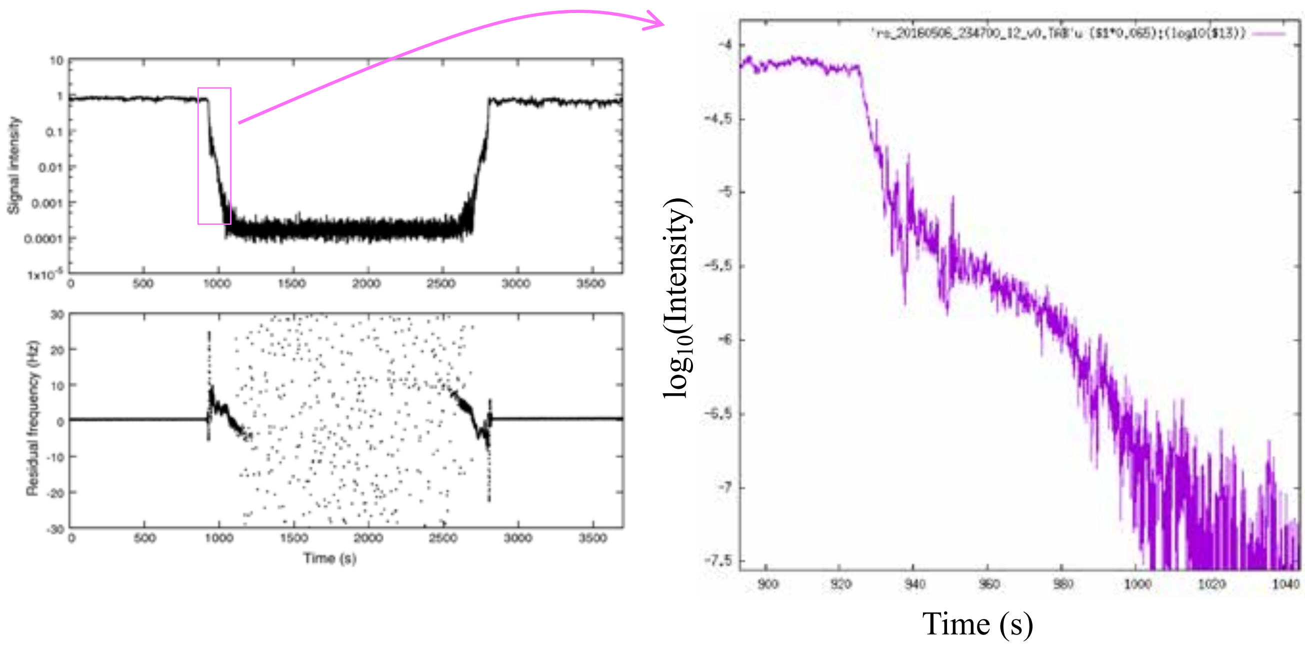

Defocusing loss

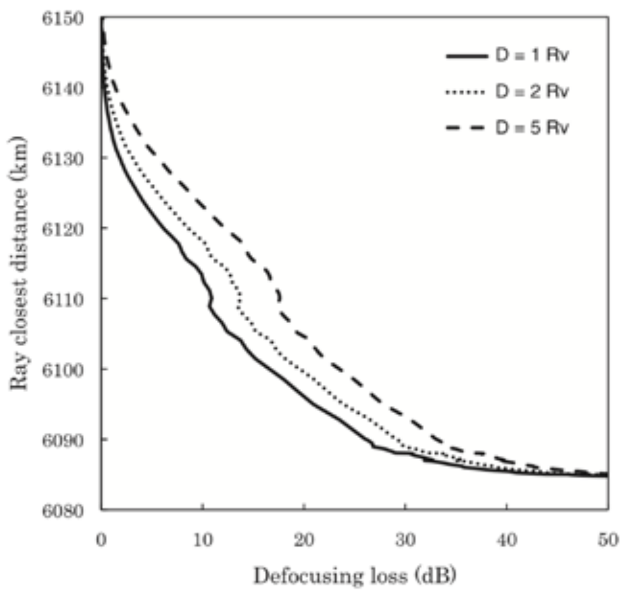

Fig. 4. Defocusing loss as a function of the ray closest distance r_0 for three distances from the spacecraft to the crossing of the ray asymptotes, D.

Imamura et al. (2011)

An example of H_2SO_4 vapor profile

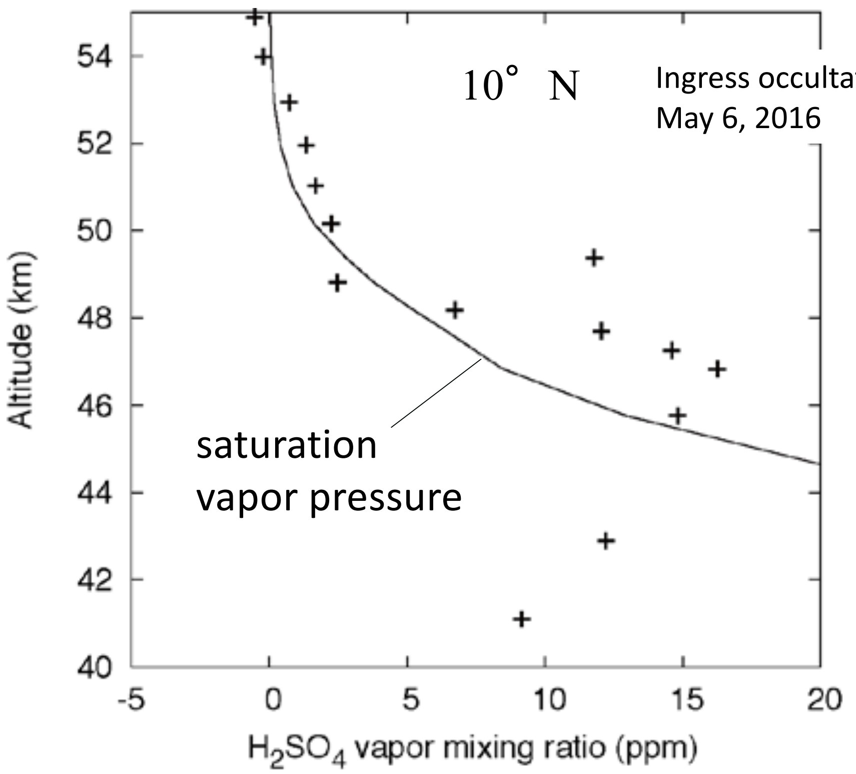

Radio scintillations caused by planetary atmospheres and the solar corona

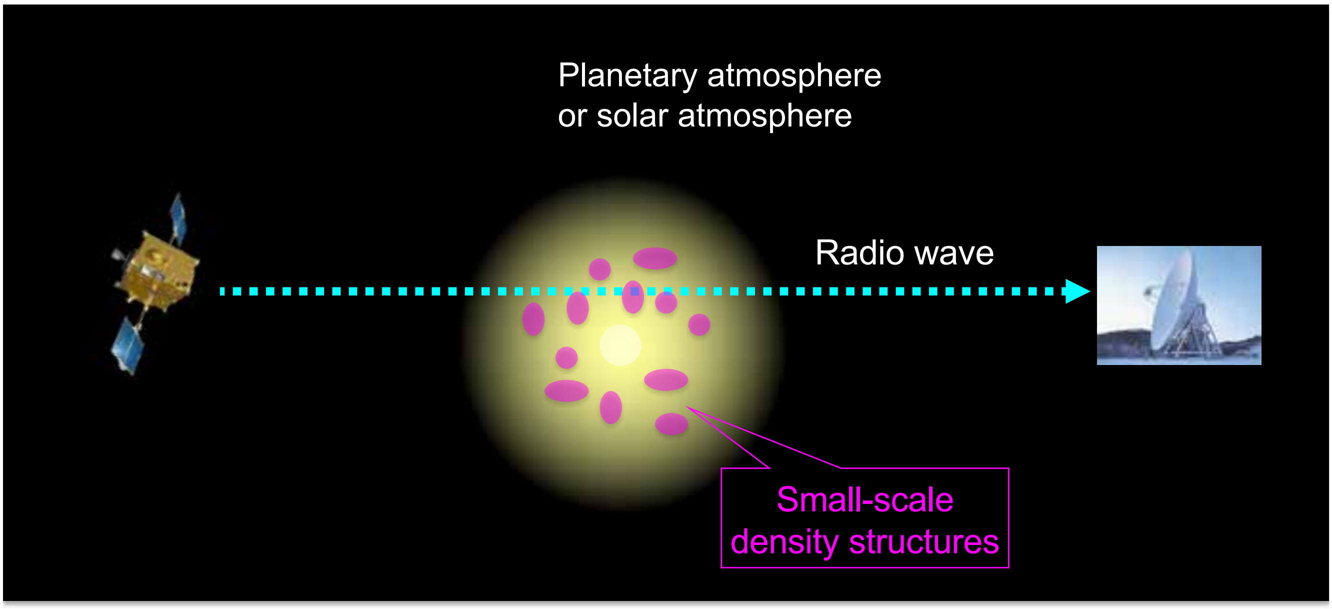

Radio scintillation measurement

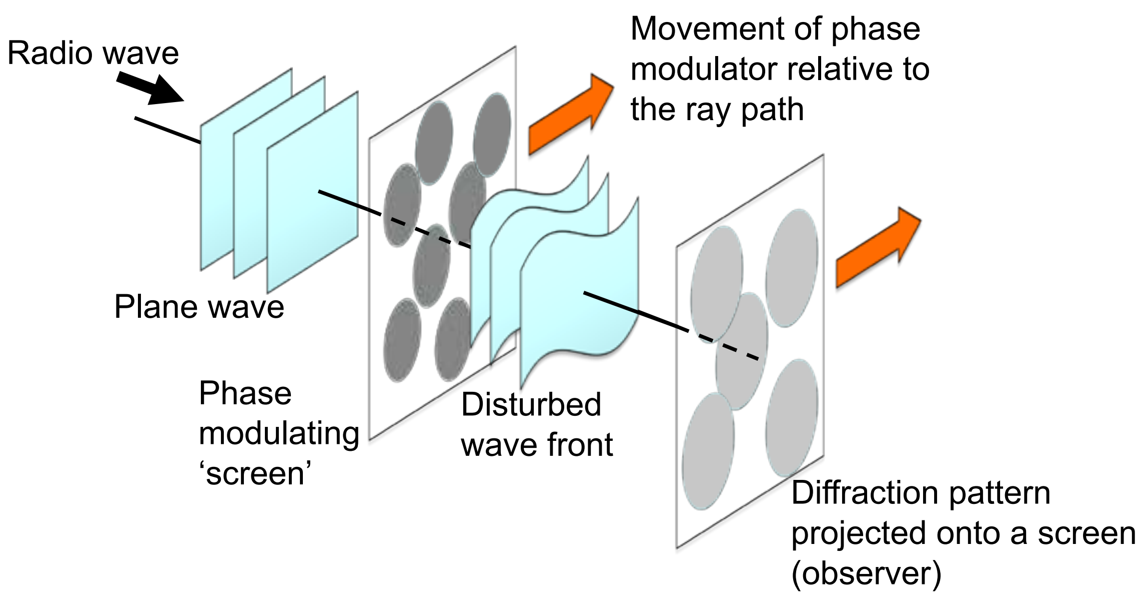

- Movement of phase modulator is caused by:
  - spacecraft motion for planetary observation
  - solar wind flow for solar observation

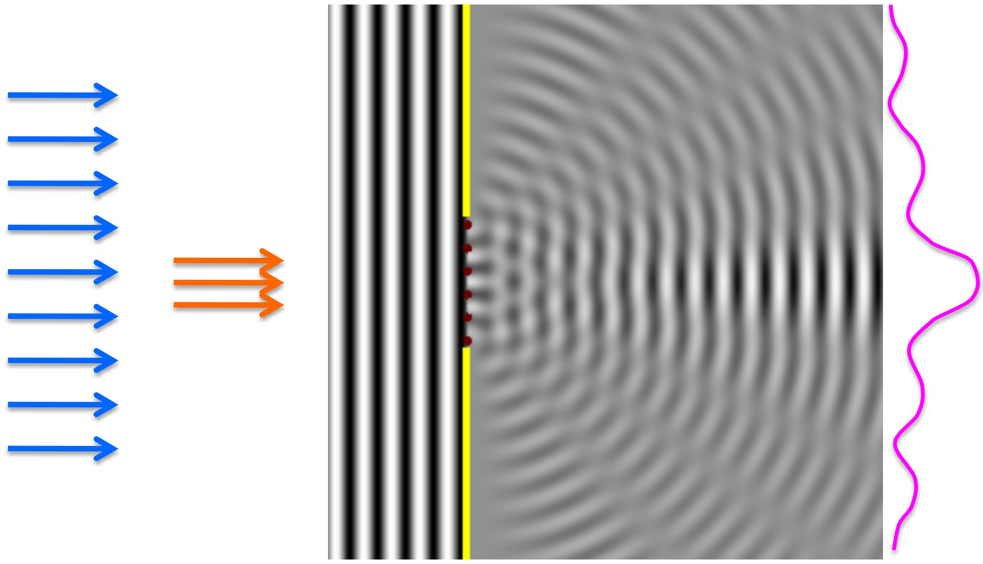

- Fresnel zone size > Phase modulator scale
  → Interference occurs
- Fresnel zone size < Phase modulator scale
  → Interference does not occur

Only small-scale structures create amplitude modulation.

Scintillation spectra

Venus atmosphere (Woo et al. 1980)

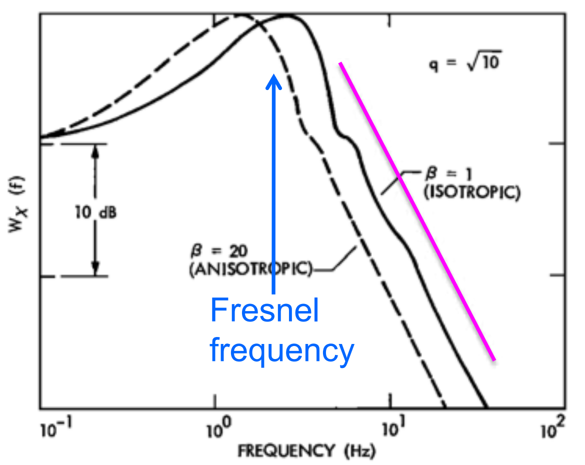

Fig. 1. Model *S* band log-amplitude power spectra, calculated fo the geometry of the 1978 DOY 356 entry occultation. Curves are com puted for a 'defocusing attenuation' of 10 dB, Kolmogorov spectrur of refractive index fluctuations, and two values for the irregularity ax ial ratio β.

Solar corona (Coles 1977)

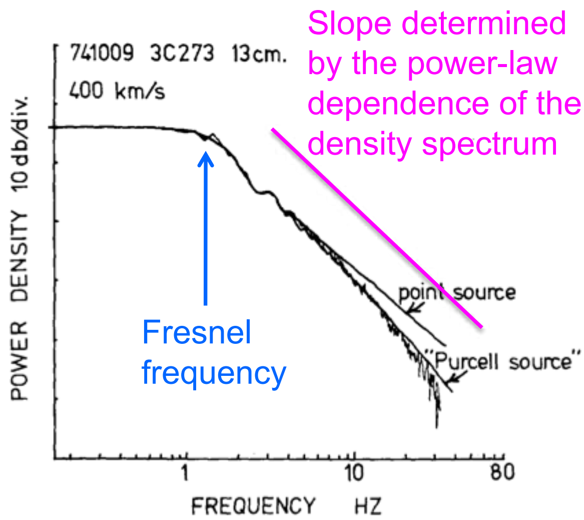

Fig. 7. A measured IPS spectrum at 13 cm from Scott (1975). The source was 3C273 on C 1974. The solid lines are computed assuming a velocity of 400 km s^{-1}, as measured from thre IPS, and a simple power-law spectrum of exponent −3.3. The effect of source diameter is sh

[Fresnel frequency] = [Velocity] / [Fresnel zone radius]

Outflow speeds of solar corona derived from Akatsuki radio occultation scintillation data

Imamura et al. (2014, ApJ)

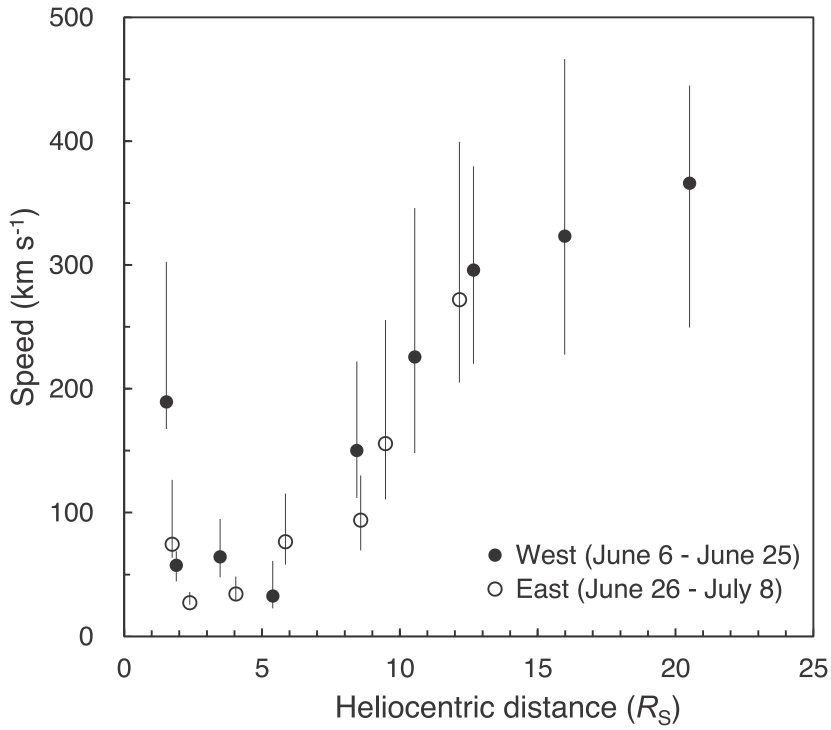

Doppler tracking of Juno spacecraft

- The spacecraft acts as a test particle falling in the gravity field of the planet. Jupiter’s gravity is inferred from range-rate measurements between a ground antenna and the spacecraft during perijove passes.
- The ground station transmits two carrier signals, at 7,153 MHz (X band) and 34,315 MHz (Ka band). On board, an X-band transponder and a Ka-band frequency translator lock the incoming carrier signals and retransmit them back to the ground station at 8,404 MHz and 32,088 MHz, respectively. The range-rate (Doppler) observable is obtained by comparing the transmitted and received frequencies.
- Spherical harmonics representation of planetary gravity fields is determined by the density distribution inside the body.

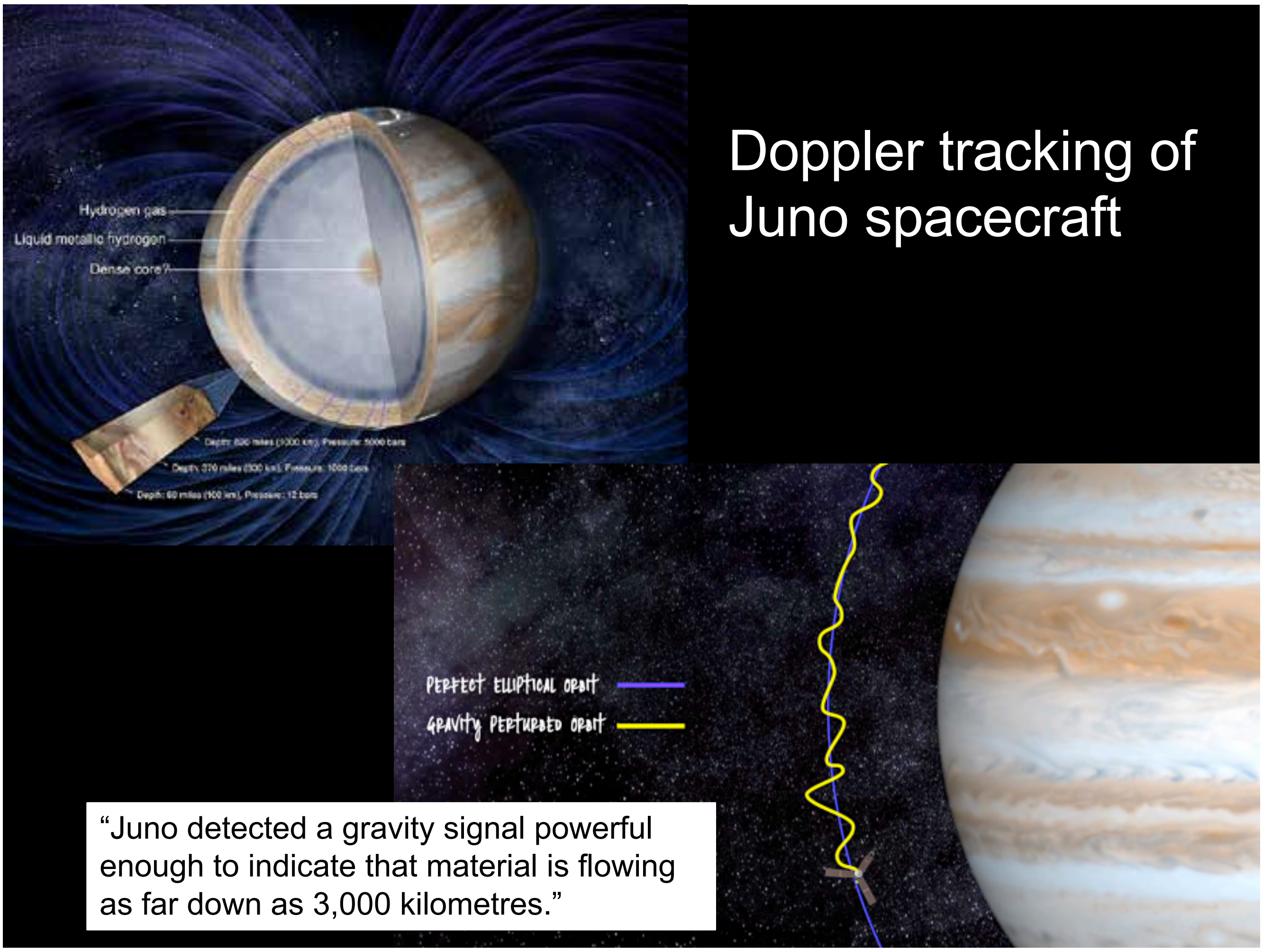

Less et al. (2018)

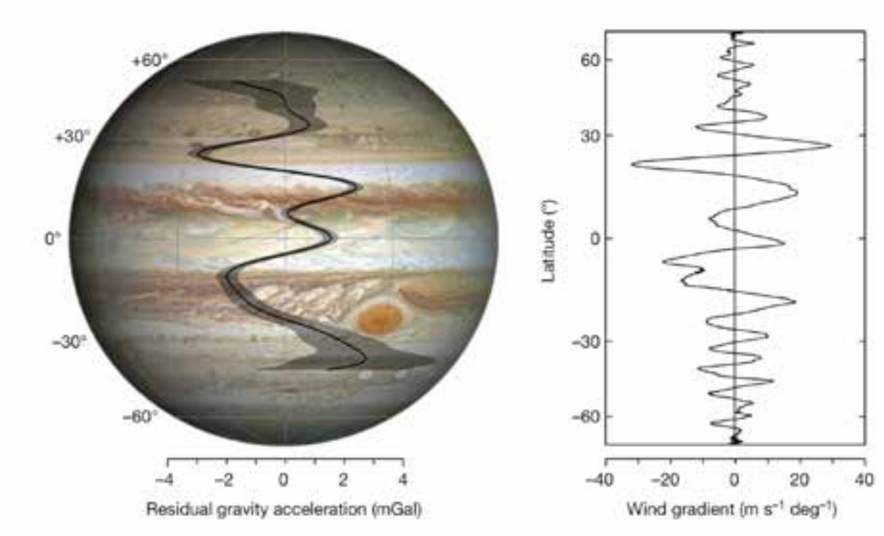

Figure 3 | Gravity disturbances due to atmospheric dynamics. a, An image of Jupiter taken by the Hubble Wide Field Camera in 2014 (https://en.wikipedia.org/wiki/Jupiter), showing the latitudinal dependence of residual gravity acceleration (in milligals, positive outwards) and associated 3σ uncertainty (shaded area) at a reference distance of 71,492 km, when the gravity from the even zonal harmonics J_2, J_4, J_6 and J_8 is removed. The residual gravity field, which is dominated by the dynamics of the flows, shows marked peaks correlated with the band structure. **b**, Latitudinal gradient of the measured wind profile. The largest (negative) peak of -3.4 ± 0.4 mGal (3σ) is found at a latitude of 24° N, where the latitudinal gradient of the wind speed reaches its largest value. The relation between the gravity disturbances and wind gradients is discussed in an accompanying paper[4].

“The observed jet streams, as they appear at the cloud level, extend down to depths of thousands of kilometres beneath the cloud level, probably to the region of magnetic dissipation at a depth of about 3,000 kilometres”

Microwave spectroscopy

ISS/SMILES for Earth's stratosphere

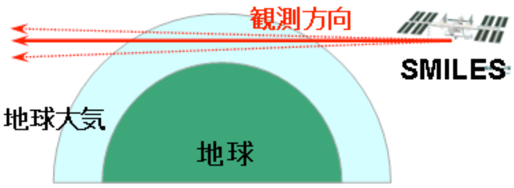

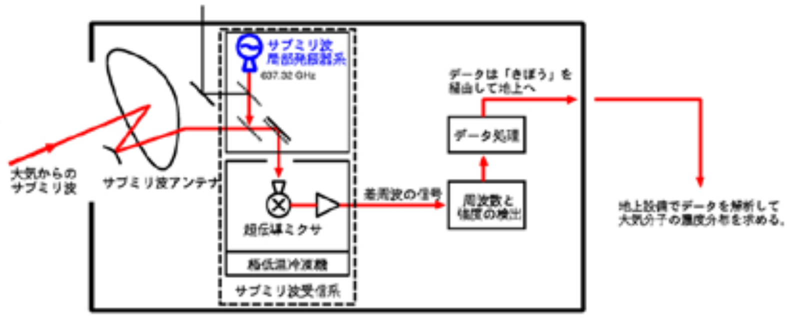

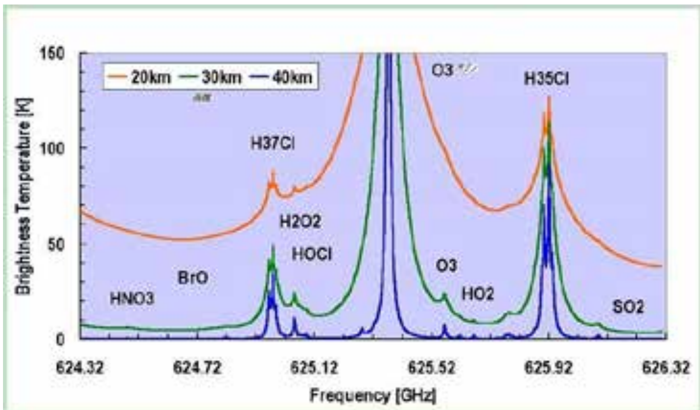

SMILES HP

ISS/SMILES for Earth's stratosphere

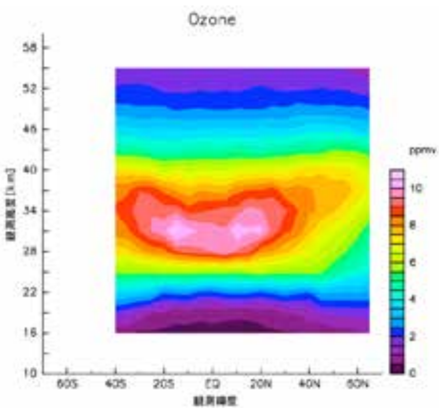

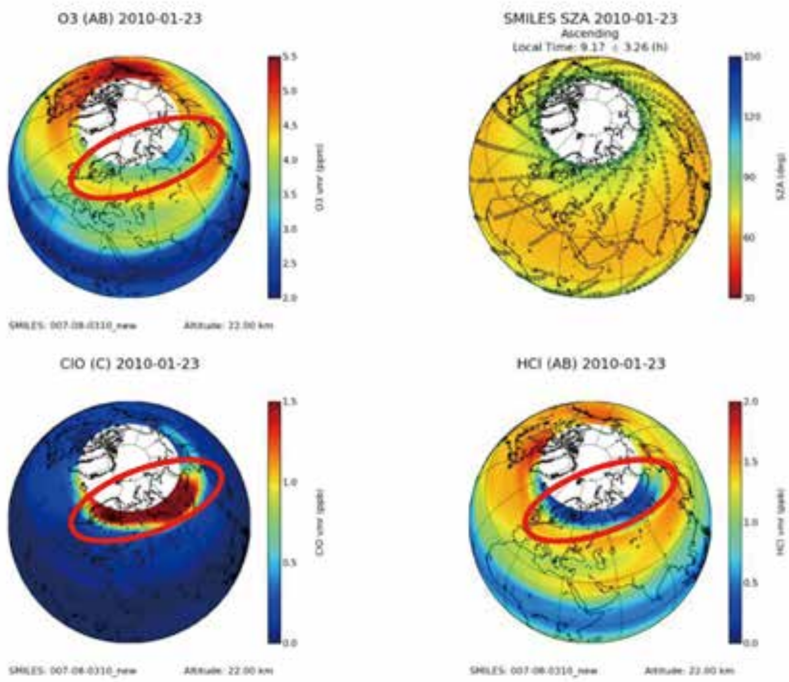

SMILES HP

JUICE(Jupiter Icy Moon Explorer)/ SWI(Submillimetre Wave Instrument)

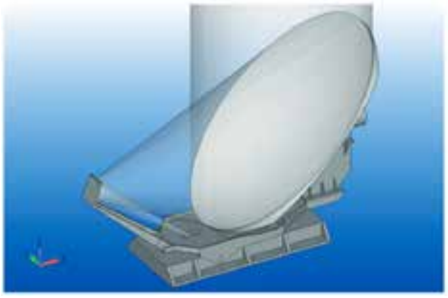

Kasai et al. (2014)

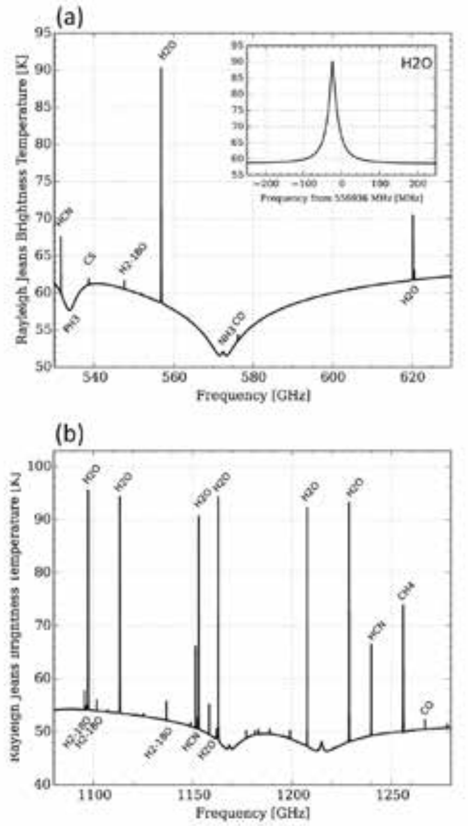

図1：SWIの観測周波数帯である(a)600 GHz帯および(b)1200 GHz帯における木星大気スペクトル(リム放射)のシミュレーション図．1000 hPaの接線高度を観測したケースを想定．(a)内部の図は，556 GHzのH_2O吸収線拡大図．木星大気の高速回転によって，吸収線の中心周波数がドップラーシフトをしている．

Microwave radiometer

JUNO/MWR

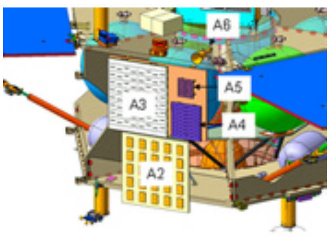

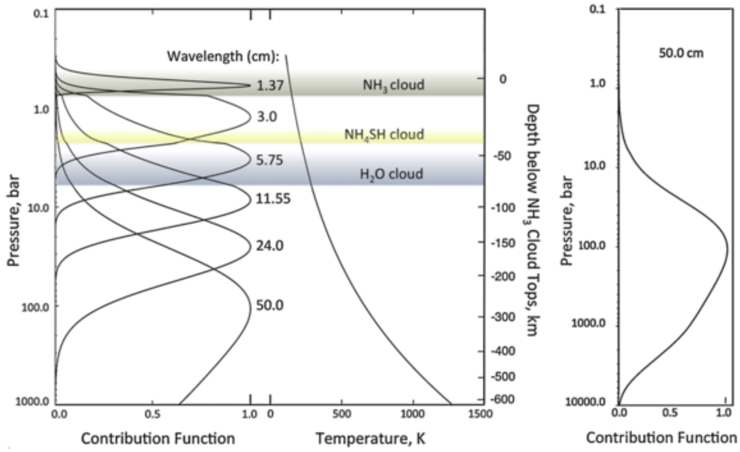

- measurements of electromagnetic waves on frequencies in the microwave range: 600 MHz, 1.2, 2.4, 4.8, 9.6 and 22 GHz, the only microwave frequencies which are able to pass through the thick Jovian atmosphere. Ammonia (NH_3) is the main opacity source.
- The radiometer will measure the abundance of water and ammonia in the deep layers of the atmosphere up to 200-bar (20 MPa; 2,900 psi) pressure or 500–600 km (310–370 mi) deep. The combination of different wavelengths and the emission angle should make it possible to obtain a temperature profile at various levels of the atmosphere.

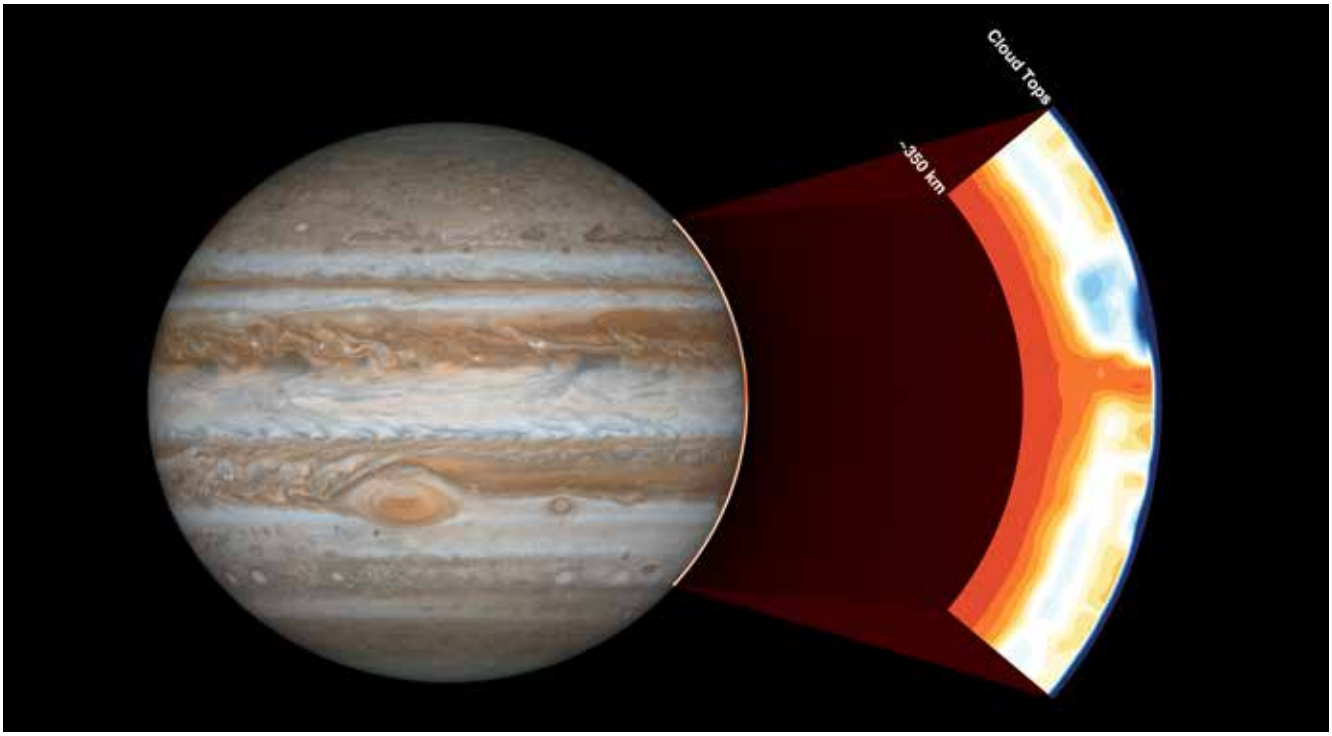

Figure 4. The colored contours show the ammonia concentration in parts per million inverted from nadir brightness temperatures during PJ1 flyby assuming that the deep water abundance is 0.06% (0.65 times solar). The deep ammonia abundance is 373 ppm, and the reference temperature is 132.1 K at 0.5 bar. The aspect ratio in the horizontal and vertical is exaggerated.